Derivation of the non-linear shallow water equations over unsaturated porous media: a discontinuous galerkin method for coarse-grained beaches

Camille Poussel, Mehmet Ersoy, Frederic Golay, Damien Sous

Derivation of the non-linear shallow water equations over unsaturated porous media: a discontinuous galerkin method for coarse-grained beaches

C. Poussel[1], M. Ersoy[1], F. Golay[1], and D. Sous[2]

[1]Institut de Mathématiques de Toulon (IMATH), Université de Toulon, La Garde, France
[2]Laboratoire des sciences pour l'ingénieur appliquées à la mécanique et au génie électrique (SIAME), Université de Pau et des Pays de l'Adour

Abstract

This work will consider the physics of free-surface flow and groundwater flow in a coupled model. Coupled models of such phenomena are not clearly justified, and there is a lack of precision in deriving such a model. The primary aim of this work is to derive a coupled model of Shallow Water Equations (SWE) and Richards' Equation (RE) using asymptotic considerations. The numerical coupling chosen for the unified model will be explained as a parallel coupling. Additionally, numerical considerations on how to solve this model using Discontinuous Galerkin (DG) methods will be provided. Furthermore, explanations will be given about how information is exchanged between the two models, which are time-synchronized. The solution of RE coupled with SWE using the mentioned procedure with DG formulation is implemented in RIVAGE (an in-house numerical code based on discontinuous Galerkin method), which is then tested on a numerical problem and validated against an experimental benchmark.

Keywords: Asymptotic analysis, Shallow water equations, Richards equation, Unsaturated porous media, Discontinuous Galerkin, Two-way coupling

Acronyms

AMR Adaptive Mesh Refinement

BB-AMR Block Based Adaptive Mesh Refinement

BDF Backward Differentiation Formula

CFL Courant-Friedrichs-Lewy

DG Discontinuous Galerkin

RE Richards' Equation

RK Runge-Kutta

RKDG Runge-Kutta Discontinuous Galerkin

SWE Shallow Water Equations

Contents

1 Introduction

The present work focuses on developing a coupled model that integrates free-surface and porous media flow models. Various methods for coupling ground and surface water flows have been extensively documented in the literature. The mathematical examination of coupling non-hydrostatic (Stokes) and single-phase Darcy flow domains can be found in several papers, including [20, 27], where the coupling is achieved through the Beavers-Joseph-Saffman interface condition [4, 22, 28]. A detailed discussion on applying these conditions to a coupled Navier-Stokes and groundwater flow is presented in [13], where a three-dimensional non-hydrostatic model is linked with Darcy flow. The authors establish the well-posedness of the model in the case of linear Stokes flow and gives an iterative method to solve the coupled system.

The field of engineering has extensively investigated various approaches to integrate depth-averaged shallow water flow equations with both single and multiphase groundwater flow equations. These models establish the connection between surface and groundwater through different methods. One approach involves approximating surface water flow using a diffusive wave approximation or Manning's equation, in conjunction with Richards' Equation (RE) for flow through the vadose zone, as outlined in [33]. This model is well-suited for

situations where flow is primarily influenced by gravity and friction, while disregarding inertial effects in the momentum equation. It is commonly utilized to simulate flow in channels and wetlands. Both Manning's equation and RE are non-linear parabolic equations in the hydraulic head (the water height above a specific reference point), resulting in the overall model being a single non-linear system that needs to be solved for water height.

An alternative approach that has been proposed involves the calculation of an "exchange flux". This approach assumes the existence of an interfacial domain that connects the two domains, referred to as the conductance concept [3, 32]. The interfacial domain is characterized by a thickness parameter and the flux is then calculated using this parameter. The exchange flux is integrated into the groundwater and surface water flow equations as source terms. One challenge of this method is the requirement for observable interfacial domains in the field [5], which makes the determination of the thickness parameter difficult. The use of the conductance concept in numerical modeling of groundwater/surface water interaction can be traced as far back as 1969 [17].

The flow model considered in this study is based on the depth-averaged, Shallow Water Equations (SWE) coupled with RE in the groundwater domain. SWE are commonly used for shallow surface water flow and thin layers of water. This model accounts for inertial effects and wetting and drying processes. When coupling these two models, a common approach found in the following literature, Dawson *et al.* 2008 [10]; Dong *et al.* 2013 [15]; Delpierre *et al.* 2023 [12]; Furman *et al.* 2008 [18]; Caviedes-Voullieme *et al.* 2012 [6]. In the SWE model, the groundwater velocity at the groundwater/surface water interface acts as a source term in the continuity equation. Pressure continuity is enforced at the interface between groundwater flow and free-surface flow. Thus, the groundwater flow equations have a time-dependent Dirichlet boundary condition at the surface water interface.

The paper is organized as follows: in Section 2, we derive a coupled model of SWE and RE using asymptotic considerations. The numerical coupling chosen for the unified model will be explained as a parallel coupling in Section 3. The solution of RE coupled with SWE using the mentioned procedure with Discontinuous Galerkin (DG) formulation is implemented in `RIVAGE`(in-house numerical code based on discontinuous Galerkin method), and tested on a numerical problem and validated against experimental benchmarks in Section 4.

2 Derivation of the coupled model

Derivation of the coupled model of RE and SWE starts by considering Navier-Stokes equations and RE on the same global domain. The model reduction from Navier-Stokes equations to SWE is carried by following derivation of SWE with varying bathymetry by Marche in 2007 [21]. In addition, ideas for handling the infiltration and recharge term in [16] are used for the following derivation.

Start by considering the incompressible Navier-Stokes system in three dimensions is given by the following system of equations:

$$\begin{cases} \operatorname{div}(\rho_0 \mathbf{u}_f) = 0 \\ \partial_t(\rho_0 \mathbf{u}_f) + \operatorname{div}(\rho_0 \mathbf{u}_f \otimes \mathbf{u}_f) - \operatorname{div}(\sigma(\mathbf{u}_f)) - \rho_0 \mathbf{F} = 0 \end{cases} \quad \text{in } \Omega_f$$

with $\mathbf{u}_f = (u_f, v_f, w_f)^T$ the velocity field ($[L \cdot T^{-1}]$), ρ_0 the fluid density ($[M \cdot L^{-3}]$) (taken to be constant since the fluid is incompressible), $\mathbf{F} = (0, 0, -g)^T$ the gravity acceleration ($[L \cdot T^{-2}]$) with g constant and $\sigma(\mathbf{u}_f)$ the total stress tensor ($[M \cdot L^{-1} \cdot T^{-2}]$) defined by :

$$\sigma(\mathbf{u}_f) = -p_f \mathbf{I} + 2\mu D(\mathbf{u}_f) \text{ with } D(u) = \frac{1}{2}\left(\nabla \mathbf{u}_f + (\nabla \mathbf{u}_f)^T\right)$$

where p_f is the pressure of fluid in the fluid domain and $\mu > 0$ the dynamic viscosity. The tensor product of two vectors $\mathbf{a} \otimes \mathbf{b}$ is defined as $\mathbf{a}\mathbf{b}^T$, and the divergence of a matrix is taken as the row-wise divergence of the matrix; in coordinates, it means:

$$(\mathrm{div}(\mathbf{A}))_i = \sum_{j=1}^{3} \partial_j A_{ij} \text{ for } i = 1, 2, 3.$$

The RE in three dimensions is given by:

$$\begin{cases} \mathbf{u}_g = -\mathbb{K}(\psi_g)\nabla h_g \\ \partial_t \theta(\psi_g) + \mathrm{div}(\mathbf{u}_g) = 0 \end{cases} \quad \text{in } \Omega_g \tag{1}$$

with $\mathbf{u}_g = (u_g, v_g, w_g)^T$ the Darcy velocity field ($[L \cdot T^{-1}]$), θ the water content ([-]), h_g the hydraulic head ($[L]$), $\mathbb{K}$ the hydraulic conductivity ($[L \cdot T^{-1}]$) and ψ_g the pressure head ($[L \cdot T^{-1}]$). In addition, the pressure head is named after its definition closely linked to p_g the pressure of fluid in the ground ($[M \cdot L^{-1} \cdot T^{-2}]$):

$$\psi_g := h_g - z = \frac{p_g}{\rho_0 g}.$$

RE is governed by θ and $\mathbb{K}$ which are two constitutive laws (interested readers can found more details in [1, 7, 9].

With numerical and practical applications in mind, an arbitrary final time $T > 0$ is considered. The *absolute height* of the surface of the water course and the *topography* of the channel bed is modeled, respectively, by the functions

$$\begin{array}{ccccc} \zeta : [0,T] \times \mathbb{R}^2 & \to & \mathbb{R} & & z_b : \mathbb{R}^2 & \to & \mathbb{R} \\ (t,x,y) & \mapsto & \zeta(t,x,y) & , & (x,y) & \mapsto & \zeta(x,y) \end{array}$$

whose values are measured with respect to a reference horizontal height of 0. The *water height* is defined by

$$h(t,x,y) := \zeta(t,x,y) - z_b(x,y).$$

The *fluid region* is defined as the area in which the fluid resides at each time $t \in [0,T]$:

$$\Omega_f(t) := \left\{(x,y,z) \in \mathbb{R}^3 \;\middle|\; z_b(x,y) < z < \zeta(t,x,y)\right\},$$

with the global fluid region

$$\Omega_f := \bigcup_{t \in [0,T]} \Omega_f(t).$$

To work with the fluid region, its indicator functions is introduced:

$$\Phi(t,x,y,z) := \mathbb{1}_{\Omega_f(t)}(x,y,z) = \mathbb{1}_{z_b(x,y)<z<\zeta(t,x,y)}, \text{ for all } (t,x,y,z) \in \mathbb{R}^4$$

The function Φ is advected by the flow so its material derivative, with respect to the flow $\mathbf{u}_f$, must be zero. Moreover, thanks to the incompressibility condition, Φ satisfies the following indicator transport equation:

$$\partial_t \Phi + \partial_x(\Phi u_f) + \partial_y(\Phi v_f) + \partial_z(\Phi w_f) = 0 \text{ on } \Omega_f. \tag{2}$$

The *ground region* is defined as the area below the topography and is fixed in time:

$$\Omega_g := \left\{(x,y,z) \in \mathbb{R}^3 \;\middle|\; z < z_b(x,y)\right\}.$$

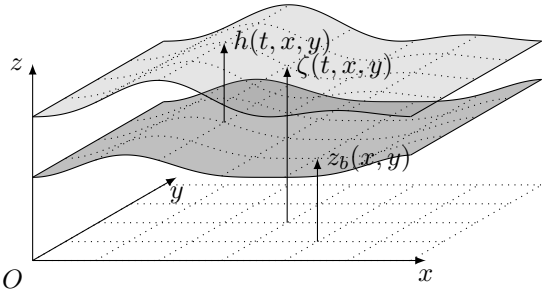

(a) Sketch of variables with h the water height, ζ the free-surface height and z_b the bathymetry

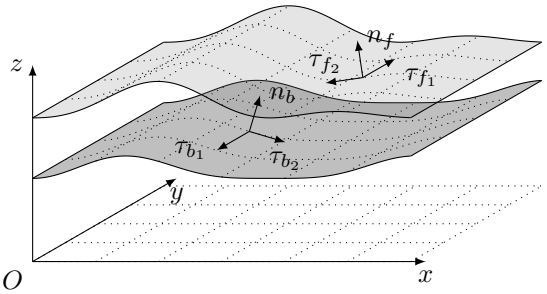

(b) Sketck of basis with $(n_b, \tau_{b_1}, \tau_{b_2})$ on the bathymetry and $(n_f, \tau_{f_1}, \tau_{f_2})$ on the free-surface

2.1 Bottom boundary condition

For the boundary between the fluid and the ground domain, multiple approach can be considered. The first one consists in considering an interfacial domain that connects the two main domains [3, 32]. An other approach consists in considering a clear boundary between the two domains [14]. In this work, the second approach is considered.

It allows to define boundary conditions on the bottom boundary. It is where interactions between the surface and the ground flow occur. Firstly, the bottom boundary domain is defined as follows:

$$\mathcal{B} := \left\{(x,y,z_b) \;\middle|\; (x,y) \in \mathbb{R}^2\right\}$$

On this boundary, the surface $\mathcal{B}$, one can define the normal vector n_b and two tangential vectors τ_{b_1} and τ_{b_2}, constituting a basis. The upward normal of $\mathcal{B}$ is defined with:

$$n_b = \frac{1}{\sqrt{1+|\nabla z_b|^2}} \begin{pmatrix} -\partial_x z_b \\ -\partial_y z_b \\ 1 \end{pmatrix}$$

and $(\tau_{b_i})_{i=1,2}$ is a basis of the tangential surface:

$$\tau_{b_1} = \frac{1}{|\nabla z_b|} \begin{pmatrix} -\partial_y z_b \\ \partial_x z_b \\ 0 \end{pmatrix} \text{ and } \tau_{b_2} = \frac{1}{\sqrt{|\nabla z_b|^2 + |\nabla z_b|^4}} \begin{pmatrix} -\partial_x z_b \\ -\partial_y z_b \\ -|\nabla z_b|^2 \end{pmatrix}$$

On the bottom boundary, two phenomena are taken into account. The first one is friction induced by the roughness of the topography. The second phenomena is friction induced by the difference between tangential fluid velocity in the fluid domain and Darcy velocity in the ground domain. The first phenomenon is taking into account through a kinematic friction law given by the following general form

$$k(\xi) := (C_{\text{lam}} + C_{\text{tur}}|\xi|), \forall \xi \in \mathbb{R}^3$$

with the non-negative friction coefficients C_{lam} and C_{tur}, respectively, the laminar and turbulent friction coefficients. The second phenomenon was greatly inspired by the work of Discacciati in 2009 [14] where he establishes a coupling between incompressible Navier Stokes equations and Darcy's law. Moreover, this kind of boundary condition originated from the work of Beavers and Joseph [4]. It results in the following Navier boundary condition:

$$(\sigma(\mathbf{u}_f)n_b) \cdot \tau_{b_i} = \left(-\rho_0 k(\mathbf{u}_f)\mathbf{u}_f + \frac{\mu \alpha_{\text{BJ}}}{\sqrt{\mathrm{k}(\psi_g)}}(\mathbf{u}_f - \mathbf{u}_g) \right) \cdot \tau_{b_i} \text{ on } \mathcal{B} \tag{3}$$

where $k(\mathbf{u}_f)$ models a general kinematic friction law on the channel bed, $\mathrm{k}(\psi_g) := \text{trace}(\mathbb{k}(\psi_g))$ and α_{BJ} is a dimensionless constant which depends on the structure of the porous medium.

Due to porosity, the ground may absorb water by infiltration or injecting water through recharge. This mechanism is modeled with the following permeable boundary condition:

$$\mathbf{u}_f(t,x,y,z) \cdot n_b = \mathbf{u}_g(t,x,y,z) \cdot n_b \text{ on } \mathcal{B} \tag{4}$$

where $\mathbf{u}_g$ is the Darcy velocity field defined in System (1). It is the influence of the ground flow to the surface flow. If $\mathbf{u}_g(t,x,y,z) \cdot n_b > 0$, water enters the fluid domain, and if $\mathbf{u}_g(t,x,y,z) \cdot n_b < 0$ water leaves the fluid domain.

Lastly, a suitable condition relating the pressure of the two fluids across $\mathcal{B}$ is needed. The balance of pressure across the interface is chosen according to the work of Discacciati [14], Girault [19] and Layton [20]:

$$-(\sigma(\mathbf{u}_f)n_b) \cdot n_b = \rho_0 g \psi_g \text{ on } \mathcal{B}. \tag{5}$$

It thus follows that Equation (3) on $\mathcal{B}$ can be rewritten as:

$$\begin{aligned}
&\mu\partial_x z_b\partial_z v_f - \mu\partial_y z_b\partial_z u_f \\
&= \Big[-\rho_0 k(\mathbf{u}_f)(-u_f\partial_y z_b + v_f\partial_x z_b) + \frac{\mu\alpha_{\mathrm{BJ}}}{\sqrt{\mathrm{k}(\psi_g)}}(-(u_f-u_g)\partial_y z_b + (v_f-v_g)\partial_x z_b)\Big]\sqrt{1+|\nabla z_b|^2} \\
&- 2\mu\partial_x z_b\partial_y z_b(\partial_x u_f - \partial_y v_f) - \mu(\partial_y z_b^2 - \partial_x z_b^2)(\partial_x v_f + \partial_y u_f) + \mu\partial_y z_b\partial_x w_f - \mu\partial_x z_b\partial_y w_f
\end{aligned} \tag{6}$$

and

$$\begin{aligned}
&\mu\partial_x z_b\partial_z u_f + \mu\partial_y z_b\partial_z v_f \\
&= \Big[\rho_0 k(\mathbf{u}_f)(-u_f\partial_x z_b - v_f\partial_y z_b - w_f|\nabla z_b|^2) \\
&- \frac{\mu\alpha_{\mathrm{BJ}}}{\sqrt{\mathrm{k}(\psi_g)}}(-(u_f-u_g)\partial_x z_b - (v_f-v_g)\partial_y z_b - (w_f-w_g)|\nabla z_b|^2)\Big]\sqrt{1+|\nabla z_b|^2} \\
&+ 2\mu\partial_x z_b^2(\partial_x u_f - \partial_z w_f) + 2\mu\partial_y z_b^2(\partial_y v_f - \partial_z w_f) + 2\mu\partial_x z_b\partial_y z_b(\partial_x v_f + \partial_y u_f) \\
&+ |\nabla z_b|^2\mu\Big(\partial_x z_b(\partial_x w_f + \partial_z u_f) - \partial_y z_b(\partial_y w_f + \partial_z v_f)\Big) + \mu\partial_x z_b\partial_x w_f + \mu\partial_y z_b\partial_y w_f
\end{aligned} \tag{7}$$

Now combining the two previous conditions :

- $\partial_x z_b$(7)-$\partial_y z_b$(6) gives an expression for $\mu|\nabla z_b|^2\partial_z u_f$:

$$\begin{aligned}
&\mu|\nabla z_b|^2\partial_z u_f \\
&= \partial_y z_b\Bigg(\Big[\rho_0 k(\mathbf{u}_f)(-u_f\partial_y z_b + v_f\partial_x z_b) - \frac{\mu\alpha_{\mathrm{BJ}}}{\sqrt{\mathrm{k}(\psi_g)}}(-(u_f-u_g)\partial_y z_b + (v_f-v_g)\partial_x z_b)\Big]\sqrt{1+|\nabla z_b|^2} \\
&+ 2\mu\partial_x z_b\partial_y z_b(\partial_x u_f - \partial_y v_f) + \mu(\partial_y z_b^2 - \partial_x z_b^2)(\partial_x v_f + \partial_y u_f) - \mu\partial_y z_b\partial_x w_f + \mu\partial_x z_b\partial_y w_f\Bigg) \\
&+ \partial_x z_b\Bigg(\Big[\rho_0 k(\mathbf{u}_f)(-u_f\partial_x z_b - v_f\partial_y z_b - w_f|\nabla z_b|^2) \\
&- \frac{\mu\alpha_{\mathrm{BJ}}}{\sqrt{\mathrm{k}(\psi_g)}}(-(u_f-u_g)\partial_x z_b - (v_f-v_g)\partial_y z_b - (w_f-w_g)|\nabla z_b|^2)\Big]\sqrt{1+|\nabla z_b|^2} \\
&+ 2\mu\partial_x z_b^2(\partial_x u_f - \partial_z w_f) + 2\mu\partial_y z_b^2(\partial_y v_f - \partial_z w_f) + 2\mu\partial_x z_b\partial_y z_b(\partial_x v_f + \partial_y u_f) \\
&+ |\nabla z_b|^2\mu\Big(\partial_x z_b(\partial_x w_f + \partial_z u_f) - \partial_y z_b(\partial_y w_f + \partial_z v_f)\Big) + \mu\partial_x z_b\partial_x w_f + \mu\partial_y z_b\partial_y w_f\Bigg);
\end{aligned}$$

- $\partial_x z_b(6)+\partial_y z_b(7)$ gives an expression for $\mu|\nabla z_b|^2\partial_z v_f$:

$$
\begin{aligned}
&\mu|\nabla z_b|^2\partial_z v_f \\
&= -\partial_x z_b\Bigg(\Big[\rho_0 k(\mathbf{u}_f)(-u_f\partial_y z_b + v_f\partial_x z_b) - \frac{\mu\alpha_{\mathrm{BJ}}}{\sqrt{\mathrm{k}(\psi_g)}}(-(u_f-u_g)\partial_y z_b + (v_f-v_g)\partial_x z_b)\Big]\sqrt{1+|\nabla z_b|^2} \\
&+ 2\mu\partial_x z_b\partial_y z_b(\partial_x u_f - \partial_y v_f) + \mu(\partial_y z_b^2 - \partial_x z_b^2)(\partial_x v_f + \partial_y u_f) - \mu\partial_y z_b\partial_x w_f + \mu\partial_x z_b\partial_y w_f\Bigg) \\
&+ \partial_y z_b\Bigg(\Big[\rho_0 k(\mathbf{u}_f)(-u_f\partial_x z_b - v_f\partial_y z_b - w_f|\nabla z_b|^2) \\
&- \frac{\mu\alpha_{\mathrm{BJ}}}{\sqrt{\mathrm{k}(\psi_g)}}(-(u_f-u_g)\partial_x z_b - (v_f-v_g)\partial_y z_b - (w_f-w_g)|\nabla z_b|^2)\Big]\sqrt{1+|\nabla z_b|^2} \\
&+ 2\mu\partial_x z_b^2(\partial_x u_f - \partial_z w_f) + 2\mu\partial_y z_b^2(\partial_y v_f - \partial_z w_f) + 2\mu\partial_x z_b\partial_y z_b(\partial_x v_f + \partial_y u_f) \\
&+ |\nabla z_b|^2\mu\Big(\partial_x z_b(\partial_x w_f + \partial_z u_f) - \partial_y z_b(\partial_y w_f + \partial_z v_f)\Big) + \mu\partial_x z_b\partial_x w_f + \mu\partial_y z_b\partial_y w_f\Bigg).
\end{aligned}
$$

In addition, Equation (4) on $\mathcal{B}$ can be rewritten as:

$$-u_f\partial_x z_b - v_f\partial_y z_b + w_f = -u_g\partial_x z_b - v_g\partial_y z_b + w_g$$

Lastly, Equation (5) on $\mathcal{B}$ can be rewritten as:

$$
\begin{aligned}
&\partial_x z_b^2 2\mu\partial_x u_f + \partial_y z_b^2 2\mu\partial_y v_f + 2\mu\partial_z w_f + 2\partial_x z_b\partial_y z_b\mu(\partial_x v_f + \partial_y u_f) \\
&- 2\partial_x z_b\mu(\partial_x w_f + \partial_z u_f) - 2\partial_y z_b\mu(\partial_y w_f + \partial_z v_f) = (p_f - \rho_0 g\psi_g)(1+|\nabla z_b|^2).
\end{aligned}
$$

2.2 Free-surface boundary condition

On the free-surface, any meteorological phenomena (such as evaporation, rainfall, wind, etc.) can be considered. Firstly, the free-surface boundary domain is defined as follows:

$$\mathfrak{F} := \big\{(t,x,y,\zeta) \;\big|\; t>0,\ (x,y)\in\mathbb{R}^2\big\}$$

On this boundary, the surface $\mathfrak{F}$ one can define the normal vector n_f and two tangential vectors τ_{f_1} and τ_{f_2}, constituting a basis. The upward normal of $\mathfrak{F}$ is defined with:

$$n_f = \frac{1}{\sqrt{1+|\nabla\zeta|^2}}\begin{pmatrix}-\partial_x\zeta\\-\partial_y\zeta\\1\end{pmatrix}$$

and $(\tau_{f_i})_{i=1,2}$ is a basis of the tangential surface:

$$\tau_{f_1} = \frac{1}{|\nabla\zeta|}\begin{pmatrix}-\partial_y\zeta\\\partial_x\zeta\\0\end{pmatrix} \text{ and } \tau_{f_2} = \frac{1}{\sqrt{|\nabla\zeta|^2+|\nabla\zeta|^4}}\begin{pmatrix}-\partial_x\zeta\\-\partial_y\zeta\\-|\nabla\zeta|^2\end{pmatrix}$$

On the free-surface, it is only considered that displacements of the free-surface advect water in the fluid domain. It gives the kinematic boundary condition:

$$\mathbf{u}_f \cdot n_f = \frac{\partial_t \zeta}{\sqrt{1+|\nabla\zeta|^2}} \text{ on } \mathfrak{F}. \tag{8}$$

Then, because no meteorological effects are considered, the stress condition of the free-surface is given by:

$$(\sigma(\mathbf{u}_f)n_f)\cdot\tau_{f_i} = 0 \text{ on } \mathfrak{F}. \tag{9}$$

One can refer to [16] for information about taking into account rainfall, and for wind stress, one can read [21].

Using definition of n_f and τ_{f_i} Equation (8) can be rewritten as:

$$\partial_t\zeta + u\partial_x\zeta + v\partial_y\zeta - w = 0.$$

In addition, Equation (9) can be rewritten as:

$$\begin{aligned}&\mu\partial_x\zeta\partial_z v_f - \mu\partial_y\zeta\partial_z u_f = \\ &-2\mu\partial_x\zeta\partial_y\zeta(\partial_x u_f - \partial_y v_f) - \mu(\partial_y\zeta^2 - \partial_x\zeta^2)(\partial_x v_f + \partial_y u_f) - \mu\partial_x\zeta\partial_y w_f + \mu\partial_y\zeta\partial_x w_f\end{aligned} \tag{10}$$

and

$$\begin{aligned}&\mu\partial_x\zeta\partial_z u_f + \mu\partial_y\zeta\partial_z v_f = \\ &2\mu\partial_x\zeta^2(\partial_x u_f - \partial_z w_f) + 2\mu\partial_y\zeta^2(\partial_y v_f - \partial_z w_f) + 2\mu\partial_x\zeta\partial_y\zeta(\partial_x v_f + \partial_y u_f) \\ &+ |\nabla\zeta|^2\mu(\partial_x\zeta(\partial_x w_f + \partial_z u_f) - \partial_y\zeta(\partial_y w_f + \partial_z v_f)) + \mu\partial_x\zeta\partial_x w_f + \mu\partial_y\zeta\partial_y w_f\end{aligned} \tag{11}$$

Now combining the two previous condition :

- $\partial_x\zeta$(11)-$\partial_y\zeta$(10) gives an expression for $\mu|\nabla\zeta|^2\partial_z u_f$:

$$\begin{aligned}&\mu|\nabla\zeta|^2\partial_z u_f \\ &= \partial_y\zeta\Big(2\mu\partial_x\zeta\partial_y\zeta(\partial_x u_f - \partial_y v_f) + \mu(\partial_y\zeta^2 - \partial_x\zeta^2)(\partial_x v_f + \partial_y u_f) + \mu\partial_x\zeta\partial_y w_f - \mu\partial_y\zeta\partial_x w_f\Big) \\ &+ \partial_x\zeta\Big(2\mu\partial_x\zeta^2(\partial_x u_f - \partial_z w_f) + 2\mu\partial_y\zeta^2(\partial_y v_f - \partial_z w_f) + 2\mu\partial_x\zeta\partial_y\zeta(\partial_x v_f + \partial_y u_f) \\ &+ |\nabla\zeta|^2\mu(\partial_x\zeta(\partial_x w_f + \partial_z u_f) - \partial_y\zeta(\partial_y w_f + \partial_z v_f)) + \mu\partial_x\zeta\partial_x w_f + \mu\partial_y\zeta\partial_y w_f\Big);\end{aligned}$$

- $\partial_x\zeta(10)+\partial_y\zeta(11)$ gives an expression for $\mu|\nabla\zeta|^2\partial_z v_f$:

$$\begin{aligned}
&\mu|\nabla\zeta|^2\partial_z v_f \\
&= -\partial_x\zeta\Big(2\mu\partial_x\zeta\partial_y\zeta(\partial_x u_f - \partial_y v_f) + \mu(\partial_y\zeta^2 - \partial_x\zeta^2)(\partial_x v_f + \partial_y u_f) + \mu\partial_x\zeta\partial_y w_f - \mu\partial_y\zeta\partial_x w_f\Big) \\
&+ \partial_y\zeta\Big(2\mu\partial_x\zeta^2(\partial_x u_f - \partial_z w_f) + 2\mu\partial_y\zeta^2(\partial_y v_f - \partial_z w_f) + 2\mu\partial_x\zeta\partial_y\zeta(\partial_x v_f + \partial_y u_f) \\
&+ |\nabla\zeta|^2\mu(\partial_x\zeta(\partial_x w_f + \partial_z u_f) - \partial_y\zeta(\partial_y w_f + \partial_z v_f)) + \mu\partial_x\zeta\partial_x w_f + \mu\partial_y\zeta\partial_y w_f\Big).
\end{aligned}$$

2.3 Dimensionless Navier-Stokes equations

To derive the Saint-Venant model, the water height is assumed small with respect to the horizontal length of the domain and that vertical variations in velocity are small compared to the horizontal variations. This is achieved by postulating a small parameter ratio:

$$\varepsilon := \frac{H}{L} = \frac{W_f}{U_f} \ll 1,$$

where H, L, V_f and U_f are, respectively, the scales of water height, domain length, vertical fluid velocity and horizontal fluid velocity. As a consequence the time scale T_f is such that:

$$T_f = \frac{L}{U_f} = \frac{H}{W_f}.$$

Moreover, for the ground domain, L, D, W_g, and U_g are the scales of, respectively, ground domain length, ground domain height, vertical ground velocity and horizontal ground velocity. As a consequence the time scale T_g is such that:

$$T_g = \frac{L}{U_g} = \frac{H}{W_g}.$$

A relation between the two time scales is needed to link the two models in the two different domains. The following relation is chosen:

$$T_f = \varepsilon^\delta T_g,$$

with $\delta \in \mathbb{R}_+^*$, a parameter that allows us to control the difference between speeds in the fluid and ground domains. It implies a set of relations between the scales of the two models:

$$U_g = \varepsilon^\delta U_f \text{ and } W_g = \varepsilon\,\varepsilon^\delta U_f.$$

The pressure scale is defined as:

$$P_f := \rho_0 U_f^2.$$

It is convenient to define the spatial characteristic length, L, and horizontal velocity, U_f (and, by definition, T_f), as finite constants with respect to $\varepsilon \to 0$, while the water height and vertical velocity are defined as $H = \varepsilon L$ and $V_f = \varepsilon U_f$,

respectively. This allows us to introduce the dimensionless quantities of time $\tilde{t}_f$, space $(\tilde{x}, \tilde{y}, \tilde{z})$, pressure $\tilde{p}_f$, and velocity field $(\tilde{u}_f, \tilde{v}_f, \tilde{w}_f)$ via the following scaling relations:

$$\left\{\begin{array}{llll} \tilde{t}_f := \dfrac{t}{T_f}, & \tilde{p}_f := \dfrac{p_f}{P_f} & \tilde{\mathbb{K}} := \mathcal{K}^{-1}\mathbb{K} & \tilde{u}_g := \dfrac{u_g}{U_g} \\ \tilde{x} := \dfrac{x}{L},\ \tilde{y} := \dfrac{y}{L}, & \tilde{u}_f := \dfrac{u_f}{U_f},\ \tilde{v}_f := \dfrac{v_f}{U_f} & \tilde{h}_g := \dfrac{h_g}{H} & \tilde{v}_g := \dfrac{v_g}{V_g} \\ \tilde{z} := \dfrac{z}{H} = \dfrac{z}{\varepsilon L}, & \tilde{w}_f := \dfrac{w_f}{V_f} = \dfrac{w_f}{\varepsilon U_f} & \tilde{\psi}_g := \dfrac{\psi_g}{H} & \tilde{w}_g := \dfrac{w_g}{W_g} \end{array}\right\}$$

with

$$\mathcal{K} = \varepsilon^{\delta} U_f \begin{pmatrix} \frac{1}{\varepsilon} & 0 & 0 \\ 0 & \frac{1}{\varepsilon} & 0 \\ 0 & 0 & \varepsilon \end{pmatrix}. \tag{12}$$

The laminar and turbulent friction factors are scaled, respectively,

$$C_{\mathrm{lam},0} := \frac{C_{\mathrm{lam}}}{V_f} = \frac{C_{\mathrm{lam}}}{\varepsilon U_f}, \quad C_{\mathrm{tur},0} := \frac{C_{\mathrm{tur}}}{\varepsilon}.$$

The dimensionless number α_{BJ} is rescaled as:

$$\alpha_{\mathrm{BJ},0} := \frac{\alpha_{\mathrm{BJ}}}{\gamma} \text{ with } \gamma = \varepsilon^{\frac{\delta+1}{2}}.$$

Finally, the following non-dimensional numbers are defined as:

$$\begin{array}{lll} \text{Froude's number,} & \mathrm{Fr} & := U_f/\sqrt{gH}, \\ \text{Reynolds number with respect to } \mu, & \mathrm{Re} & := \rho_0 U_f L/\mu. \end{array}$$

Using these dimensionless variables in the Navier-Stokes equations and re-ordering the term with respect to power of ε, the dimensionless incompressible Navier-Stokes equations reads as follows:

$$\left\{\begin{array}{l} \mathrm{div}_{\tilde{x}\tilde{y}}(\tilde{\mathbf{u}}_f) + \partial_{\tilde{z}}\tilde{w}_f = 0 \\ \partial_{\tilde{t}}\tilde{\mathbf{u}}_f + \mathrm{div}_{\tilde{x}\tilde{y}}(\tilde{\mathbf{u}}_f \otimes \tilde{\mathbf{u}}_f) + \partial_{\tilde{z}}(\tilde{w}_f\tilde{\mathbf{u}}_f) + \nabla_{\tilde{x}\tilde{y}}\tilde{p}_f = \\ \qquad \mathrm{Re}^{-1}\left(2\mathrm{div}_{\tilde{x}\tilde{y}}(D_{\tilde{x}\tilde{y}}(\tilde{\mathbf{u}}_f)) + \nabla_{\tilde{x}\tilde{y}}(\partial_{\tilde{z}}\tilde{w}_f) + \dfrac{1}{\varepsilon}\partial_{\tilde{z}\tilde{z}}\tilde{\mathbf{u}}_f\right) \\ \partial_{\tilde{z}}\tilde{p}_f = \mathrm{Re}^{-1}\left(\varepsilon^2\Delta_{\tilde{x}\tilde{y}}\tilde{w}_f + \mathrm{div}_{\tilde{x}\tilde{y}}(\partial_{\tilde{z}}\tilde{\mathbf{u}}_f) + 2\partial_{\tilde{z}\tilde{z}}\tilde{w}_f\right) \\ \qquad -\varepsilon^2\Big(\partial_{\tilde{t}}\tilde{w}_f + \mathrm{div}_{\tilde{x}\tilde{y}}(\tilde{w}_f\tilde{\mathbf{u}}_f) + \partial_{\tilde{z}}(\tilde{w}_f^2)\Big) - \mathrm{Fr}^{-2} \end{array}\right. \tag{13}$$

with $\tilde{\mathbf{u}}_f = (\tilde{u}_f, \tilde{v}_f)^T$, $\nabla_{\tilde{x}\tilde{y}} = (\partial_{\tilde{x}}, \partial_{\tilde{y}})^T$, $D_{\tilde{x}\tilde{y}}(\mathbf{a}) = ((\nabla_{\tilde{x}\tilde{y}}\mathbf{a}) + (\nabla_{\tilde{x}\tilde{y}}\mathbf{a})^T)/2$, $\forall \mathbf{a} \in \mathbb{R}^2$ and $\Delta_{\tilde{x}\tilde{y}}a = \partial_{\tilde{x}\tilde{x}}a + \partial_{\tilde{y}\tilde{y}}a$, $\forall a \in \mathbb{R}$. Then, using the same dimensionless relations, RE reads as follows:

$$\partial_{\tilde{t}}\theta(H\tilde{\psi}_g) + \partial_{\tilde{x}}\tilde{u}_g + \partial_{\tilde{y}}\tilde{v}_g + \partial_{\tilde{z}}\tilde{w}_g = 0 \tag{14}$$

On the fluid boundary $\mathcal{B}$, the dimensionless Navier boundary condition 3 and with the expression of $\mu|\nabla z_b|^2\partial_z u_f$, implies that

$$\begin{aligned} \frac{\partial_{\tilde{z}}\tilde{u}_f}{\varepsilon^2\mathrm{Re}} = &-\left(C_{\mathrm{lam},0} + C_{\mathrm{tur},0}\sqrt{\tilde{u}_f^2 + \tilde{v}_f^2}\right)\tilde{u}_f \\ &+ \frac{1}{\sqrt{\varepsilon}\sqrt{\mathrm{Re}}\mathrm{Fr}}\frac{\alpha_{\mathrm{BJ},0}}{\sqrt{\tilde{K}_x + \tilde{K}_y}}(\tilde{u}_f - \varepsilon^{\delta}\tilde{u}_g) + O(\mathrm{Re}^{-1}) + O(\varepsilon^2). \end{aligned}$$

Similarly the dimensionless Navier boundary condition 3 with the expression of $\mu|\nabla z_b|^2\partial_z v_f$

$$\begin{aligned}\frac{\partial_{\tilde{z}}\tilde{v}_f}{\varepsilon^2\mathrm{Re}} =& -\left(C_{\mathrm{lam},0}+C_{\mathrm{tur},0}\sqrt{\tilde{u}_f^2+\tilde{v}_f^2}\right)\tilde{v}_f \\ &+\frac{1}{\sqrt{\varepsilon}\sqrt{\mathrm{Re}}\mathrm{Fr}}\frac{\alpha_{\mathrm{BJ},0}}{\sqrt{\tilde{K}_x+\tilde{K}_y}}(\tilde{v}_f-\varepsilon^\delta\tilde{v}_g)+O(\mathrm{Re}^{-1})+O(\varepsilon^2).\end{aligned}$$

The dimensionless permeable boundary condition 4 implies that on $\mathcal{B}$

$$-\tilde{u}_f\partial_{\tilde{x}}\tilde{z}_b-\tilde{v}_f\partial_{\tilde{y}}\tilde{z}_b+\tilde{w}_f=-\varepsilon^\delta\tilde{u}_g\partial_{\tilde{x}}\tilde{z}_b-\varepsilon^\delta\tilde{v}_g\partial_{\tilde{y}}\tilde{z}_b+\varepsilon^\delta\tilde{w}_g \tag{15}$$

The dimensionless balance of pressure 5 implies that on $\mathcal{B}$

$$\tilde{p}_f=\frac{1}{\mathrm{Fr}^2}\tilde{\psi}_g-\mathrm{Re}^{-1}(2\partial_{\tilde{x}}\tilde{z}_b\partial_{\tilde{z}}\tilde{u}_f+2\partial_{\tilde{y}}\tilde{z}_b\partial_{\tilde{z}}\tilde{v}_f-2\partial_{\tilde{z}}\tilde{w}_f)+O(\varepsilon^2)$$

The dimensionless kinematic boundary condition 8 implies that on $\mathfrak{F}$

$$\partial_{\tilde{t}}\tilde{\zeta}+\tilde{u}_f\partial_{\tilde{x}}\tilde{\zeta}+\tilde{v}_f\partial_{\tilde{y}}\tilde{\zeta}-\tilde{w}_f=0 \tag{16}$$

The dimensionless stress boundary condition 9 implies that on $\mathfrak{F}$

$$\frac{\partial_{\tilde{z}}\tilde{u}_f}{\varepsilon^2\mathrm{Re}}=O(\mathrm{Re}^{-1}) \text{ and } \frac{\partial_{\tilde{z}}\tilde{v}_f}{\varepsilon^2\mathrm{Re}}=O(\mathrm{Re}^{-1}).$$

2.4 First order approximation of the dimensionless Navier-Stokes equations

Dropping all the term of $O(\varepsilon)$ and above in Equation (13), the hydrostatic approximation is deduced from the dimensionless Navier-Stokes system

$$\begin{aligned}\mathrm{div}_{\tilde{x}\tilde{y}}(\tilde{\mathbf{u}}_f)+\partial_{\tilde{z}}\tilde{w}_f&=0\\ \partial_{\tilde{t}}\tilde{\mathbf{u}}_f+\mathrm{div}_{\tilde{x}\tilde{y}}(\tilde{\mathbf{u}}_f\otimes\tilde{\mathbf{u}}_f)+\partial_{\tilde{z}}\left[\tilde{w}_f\tilde{\mathbf{u}}_f\right]+\nabla_{\tilde{x}\tilde{y}}\tilde{p}_f&=\mathrm{Re}^{-1}\Big(2\mathrm{div}_{\tilde{x}\tilde{y}}(D_{\tilde{x}\tilde{y}}(\tilde{\mathbf{u}}_f))+\frac{1}{\varepsilon^2}\partial_{\tilde{z}\tilde{z}}\tilde{\mathbf{u}}_f+\partial_{\tilde{z}}\left[\nabla_{\tilde{x}\tilde{y}}(\tilde{w}_f)\right]\Big)\\ \partial_{\tilde{z}}\tilde{p}_f&=\mathrm{Re}^{-1}\Big(\partial_{\tilde{z}}\left[\mathrm{div}_{\tilde{x}\tilde{y}}(\tilde{\mathbf{u}}_f)\right]+2\partial_{\tilde{z}\tilde{z}}\tilde{w}_f\Big)-\mathrm{Fr}^{-2}\end{aligned}$$

Then the vertical averaging is considered valid in a turbulent regime the following asymptotic setting is considered

$$\mathrm{Re}^{-1}=\varepsilon. \tag{17}$$

By using this new assumption, and dropping all the term of $O(\varepsilon)$ it gives:

$$\begin{aligned}\mathrm{div}_{\tilde{x}\tilde{y}}(\tilde{\mathbf{u}}_f)+\partial_{\tilde{z}}\tilde{w}_f&=0\\ \partial_{\tilde{t}}\tilde{\mathbf{u}}_f+\mathrm{div}_{\tilde{x}\tilde{y}}(\tilde{\mathbf{u}}_f\otimes\tilde{\mathbf{u}}_f)+\partial_{\tilde{z}}\left[\tilde{w}_f\tilde{\mathbf{u}}_f\right]+\nabla_{\tilde{x}\tilde{y}}\tilde{p}_f&=\partial_{\tilde{z}}\left[\frac{1}{\varepsilon}\partial_{\tilde{z}}\tilde{\mathbf{u}}_f\right]\\ \partial_{\tilde{z}}\tilde{p}_f&=-\mathrm{Fr}^{-2}\end{aligned}$$

Then by dropping $\tilde{\square}$ the previous system becomes

$$\partial_x u_{f,\varepsilon} + \partial_y u_{f,\varepsilon} + \partial_z w_{f,\varepsilon} = 0, \tag{18}$$

$$\partial_t u_{f,\varepsilon} + \partial_x \left[u_{f,\varepsilon}^2\right] + \partial_y \left[u_{f,\varepsilon} v_{f,\varepsilon}\right] + \partial_z \left[u_{f,\varepsilon} w_{f,\varepsilon}\right] + \partial_x p_{f,\varepsilon} = \partial_z \left[\frac{1}{\varepsilon}\partial_z u_{f,\varepsilon}\right], \tag{19}$$

$$\partial_t v_{f,\varepsilon} + \partial_x \left[u_{f,\varepsilon} v_{f,\varepsilon}\right] + \partial_y \left[v_{f,\varepsilon}^2\right] + \partial_z \left[v_{f,\varepsilon} w_{f,\varepsilon}\right] + \partial_y p_{f,\varepsilon} = \partial_z \left[\frac{1}{\varepsilon}\partial_z v_{f,\varepsilon}\right], \tag{20}$$

$$\partial_z p_{f,\varepsilon} = -\mathrm{Fr}^{-2} \tag{21}$$

with $(u_{f,\varepsilon}, v_{f,\varepsilon}, w_{f,\varepsilon}, p_{f,\varepsilon})$ the solution of the first-order dimensionless Navier-Stokes system.

Similarly for (14) it gives :

$$\partial_t \theta(H\psi_g) + \partial_{\tilde{x}} u_g + \partial_y v_g + \partial_z w_g = 0$$

with $(u_{g,\varepsilon}, v_{g,\varepsilon}, w_{g,\varepsilon}, \psi_{g,\varepsilon}, h_{g,\varepsilon})$ the solution of the first-order dimensionless Richards'equation. Boundary conditions on $\mathcal{B}$ under the first-order approximation and 17 are

$$\begin{aligned}
\frac{1}{\varepsilon}\partial_z \mathbf{u}_{f,\varepsilon} &= -k_0(\mathbf{u}_{f,\varepsilon})\mathbf{u}_{f,\varepsilon} + \frac{\mathrm{Fr}^{-1}\alpha_{\mathrm{BJ},0}}{\sqrt{K_x + K_y}}(\mathbf{u}_{f,\varepsilon} - \varepsilon^\delta \mathbf{u}_{g,\varepsilon}) && \text{on } \mathcal{B},\\
u_{f,\varepsilon}\partial_x z_b v_{f,\varepsilon}\partial_y z_b - w_{f,\varepsilon} &= \varepsilon^\delta u_{g,\varepsilon}\partial_x z_b + \varepsilon^\delta v_{g,\varepsilon}\partial_y z_b - \varepsilon^\delta w_{g,\varepsilon} && \text{on } \mathcal{B},\\
p_{f,\varepsilon} &= \frac{1}{\mathrm{Fr}^2}\psi_{g,\varepsilon} && \text{on } \mathcal{B}
\end{aligned} \tag{22}$$

with $\mathbf{u}_{f,\varepsilon} = (u_{f,\varepsilon}, v_{f,\varepsilon})^T$,$\mathbf{u}_{g,\varepsilon} = (u_{g,\varepsilon}, v_{g,\varepsilon})^T$ and $k_0(\mathbf{u}_{f,\varepsilon}) := C_{\mathrm{lam},0} + C_{\mathrm{tur},0}|\mathbf{u}_{f,\varepsilon}|$. Boundary conditions on $\mathfrak{F}$ under the first-order approximation and 17 are

$$\frac{1}{\varepsilon}\partial_z \mathbf{u}_{f,\varepsilon} = 0 \text{ on } \mathfrak{F}, \tag{23}$$

$$\partial_t \zeta + u_{f,\varepsilon}\partial_x \zeta + v_{f,\varepsilon}\partial_y \zeta - w_{f,\varepsilon} = 0 \text{ on } \mathfrak{F}. \tag{24}$$

Vertically integrating both members of 21 between z and $\zeta(t,x,y)$, the hydrostatic pressure is obtained

$$\begin{aligned}
\int_z^\zeta \partial_z p_{f,\varepsilon} dz &= -\int_z^\zeta \mathrm{Fr}^{-2} dz\\
p_{f,\varepsilon}(t,x,y,\zeta) - p_{f,\varepsilon}(t,x,y,z) &= -\mathrm{Fr}^{-2}(\zeta(t,x,y) - z)
\end{aligned}$$

Assuming that the pressure exerted on the free-surface $p_{f,\varepsilon}(t,x,y,\zeta) = p_{\mathrm{atm}}$ for some constant $p_{\mathrm{atm}} \in \mathbb{R}$ (all other meteorological phenomena are neglected), this becomes

$$p_{f,\varepsilon}(t,x,y,z) = \mathrm{Fr}^{-2}(\zeta(t,x,y) - z) + p_{\mathrm{atm}} \tag{25}$$

If Equation (2) is integrated between $z = z_b(x,y)$ and $z = \zeta(t,x,y)$ it gives:

$$\begin{aligned}
&\int_{z_b}^\zeta \partial_t \Phi dz + \int_{z_b}^\zeta \partial_x(\Phi u_{f,\varepsilon})dz + \int_{z_b}^\zeta \partial_y(\Phi v_{f,\varepsilon})dz + \int_{z_b}^\zeta \partial_z(\Phi w)dz = 0\\
\iff &\partial_t h(t,x,y) + \partial_x\left(\int_{z_b}^\zeta u_{f,\varepsilon}dz\right) + \partial_y\left(\int_{z_b}^\zeta v_{f,\varepsilon}dz\right) + \left(u_{f,\varepsilon}\partial_x z_b + v_{f,\varepsilon}\partial_y z_b - w\right)|_{z=z_b}\\
&- \left(\partial_t\zeta + u_{f,\varepsilon}\partial_x\zeta + v_{f,\varepsilon}\partial_y\zeta - w\right)|_{z=\zeta} = 0
\end{aligned}$$

Using Equation (15) and Equation (16) gives:

$$\partial_t h(t,x,y) + \partial_x \left(\int_{z_b}^{\zeta} u dz \right) + \partial_y \left(\int_{z_b}^{\zeta} v dz \right) = -\varepsilon^{\delta} u_{g,\varepsilon} \partial_x z_b - \varepsilon^{\delta} v_{g,\varepsilon} \partial_y z_b + \varepsilon^{\delta} w_{g,\varepsilon}.$$

Noting $\bar{f}$ as the mean of a generic function f over the section $[z_b(x,y), \zeta(t,x,y)]$,

$$\bar{f}(t,x,y) = \frac{1}{h(t,x,y)} \int_{z_b(x,y)}^{\zeta(t,x,y)} f(t,x,y,\eta) d\eta,$$

Using the following approximations:

$$u_{f,\varepsilon}(t,x,y,z) = \bar{u}_{\varepsilon} + O(\varepsilon) \text{ and } \overline{u_{f,\varepsilon}^2} = \bar{u}_{\varepsilon}^2 + O(\varepsilon),$$

and dropping the first higher order terms in ε gives mass-balance equation:

$$\partial_t [h] + \partial_x [h\bar{u}_{\varepsilon}] + \partial_y [h\bar{v}_{\varepsilon}] = -\varepsilon^{\delta} u_{g,\varepsilon} \partial_x z_b - \varepsilon^{\delta} v_{g,\varepsilon} \partial_y z_b + \varepsilon^{\delta} w_{g,\varepsilon}. \tag{26}$$

Integrating 19 between $z = z_b(x,y)$ and $z = \zeta(t,x,y)$ gives:

$$\begin{aligned}
&\partial_t \int_{z_b}^{\zeta} u_{f,\varepsilon} dz + \partial_x \int_{z_b}^{\zeta} \left[u_{f,\varepsilon}^2 \right] dz + \partial_y \int_{z_b}^{\zeta} \left[u_{f,\varepsilon} v_{f,\varepsilon} \right] dz + \partial_x \int_{z_b}^{\zeta} p_{f,\varepsilon} dz \\
&- (p_{f,\varepsilon} \partial_x \zeta)|_{\zeta} + (p_{f,\varepsilon} \partial_x z_b)|_{z_b} \\
&- \left(\Big(\partial_t \zeta + u_{f,\varepsilon} \partial_x \zeta + v_{f,\varepsilon} \partial_y \zeta - w_{f,\varepsilon} \Big) u_{f,\varepsilon} \right)|_{\zeta} + \left(\Big(u_{f,\varepsilon} \partial_x z_b + v_{f,\varepsilon} \partial_y z_b + w_{f,\varepsilon} \Big) u_{f,\varepsilon} \right)|_{z_b} \\
&= \left[\frac{1}{\varepsilon} \partial_z u_{f,\varepsilon} \right]_{z_b}^{\zeta}
\end{aligned}$$

Using Equation (25) for the previous equations it gives:

$$\int_{z_b}^{\zeta} p_{f,\varepsilon} dz = \mathrm{Fr}^{-2} \frac{h^2}{2}$$

with $p_{\mathrm{atm}} = 0$. Replacing previous terms in the integration gives:

$$\begin{aligned}
&\partial_t [h\bar{u}_{\varepsilon}] + \partial_x \left[h\bar{u}_{\varepsilon}^2 + \frac{h^2}{2\mathrm{Fr}^2} \right] + \partial_y [h\bar{u}_{\varepsilon}\bar{v}_{\varepsilon}] = -\frac{1}{\mathrm{Fr}^2} h \partial_x [z_b] \\
&- k_0(\mathbf{u}_{f,\varepsilon}) u_{f,\varepsilon} + \frac{\mathrm{Fr}^{-1} \alpha_{\mathrm{BJ},0}}{\sqrt{K_x + K_y}} (u_{f,\varepsilon} - \varepsilon^{\delta} u_{g,\varepsilon}) + (-\varepsilon^{\delta} u_{g,\varepsilon} \partial_x z_b - \varepsilon^{\delta} v_{g,\varepsilon} \partial_y z_b + \varepsilon^{\delta} w_{g,\varepsilon}) u_{f,\varepsilon}
\end{aligned} \tag{27}$$

Similarly integrating Equation (20) between $z = z_b(x,y)$ and $z = \zeta(t,x,y)$ gives:

$$\begin{aligned}
&\partial_t [h\bar{v}_{\varepsilon}] + \partial_x [h\bar{u}_{\varepsilon}\bar{v}_{\varepsilon}] + \partial_y \left[h\bar{v}_{\varepsilon}^2 + \frac{h^2}{2\mathrm{Fr}^2} \right] = -\frac{1}{\mathrm{Fr}^2} h \partial_y [z_b] \\
&- k_0(\mathbf{u}_{f,\varepsilon}) v_{f,\varepsilon} + \frac{\mathrm{Fr}^{-1} \alpha_{\mathrm{BJ},0}}{\sqrt{K_x + K_y}} (v_{f,\varepsilon} - \varepsilon^{\delta} v_{g,\varepsilon}) + (-\varepsilon^{\delta} u_{g,\varepsilon} \partial_x z_b - \varepsilon^{\delta} v_{g,\varepsilon} \partial_y z_b + \varepsilon^{\delta} w_{g,\varepsilon}) v_{f,\varepsilon}
\end{aligned} \tag{28}$$

Finally by dropping the average $\bar{\square}$ notation and considering the mass balance equation 26 and momentum equations 27 and 28 the dimensionless Saint-Venant system with recharge is obtained:

$$\begin{cases} \partial_t [h] + \partial_x [hu_f] + \partial_y [hv_f] \\ \qquad = \varepsilon^\delta(-u_g\partial_x z_b - v_g\partial_y z_b + w_g) \\ \partial_t [hu_f] + \partial_x \left[hu_f^2 + \dfrac{h^2}{2\mathrm{Fr}^2}\right] + \partial_y [hu_f v_f] = -\dfrac{1}{\mathrm{Fr}^2} h\partial_x [z_b] \\ \qquad - k_0(u_f, v_f)u_f + \dfrac{\mathrm{Fr}^{-1}\alpha_{\mathrm{BJ},0}}{\sqrt{K_x + K_y}}(u_f - \varepsilon^\delta u_g) + \varepsilon^\delta(-u_g\partial_x z_b - v_g\partial_y z_b + w_g)u_f \\ \partial_t [hv_f] + \partial_x [hu_f v_f] + \partial_y \left[hv_f^2 + \dfrac{h^2}{2\mathrm{Fr}^2}\right] = -\dfrac{1}{\mathrm{Fr}^2} h\partial_y [z_b] \\ \qquad - k_0(u_f, v_f)v_f + \dfrac{\mathrm{Fr}^{-1}\alpha_{\mathrm{BJ},0}}{\sqrt{K_x + K_y}}(v_f - \varepsilon^\delta v_g) + \varepsilon^\delta(-u_g\partial_x z_b - v_g\partial_y z_b + w_g)v_f \end{cases} \tag{29}$$

For now, ε^δ is kept on purpose in the Shallow-Water system of equations. ε^δ are used to show that the influence of ground flow on free-surface flow is valid with the first order of approximation only for specific values of δ. Since for establishing the classic Shallow-Water system, terms of order greater than ε are dropped, terms of order ε^δ are considered for $0 \leq \delta < 1$.

If δ is chosen in this range, the two-way coupling is valid if ground fluid speeds are not too small compared to free-surface fluid speeds. In other words, if the time scale for the two models is similar. Moreover, one can see that the rescaling of the hydraulic conductivity tensor is expressed with U_f and ε^δ. Since hydraulic conductivity is fixed for a given problem, the two-way coupling is valid for a specific range of fluid speeds. As depicted in [9] for instance, hydraulic conductivity is relatively minor for most materials. The two way coupling is valid for a whole range of permeability, as long as the characteristic time of the problem is adequate. For instance for almost impervious materials, slow-evolving problems such as tides, water recharge, rain, or snow melting must be considered. In addition, for more permeable materials fast-evolving problems such as waves swashing on a sand beach, overland flow, and flooding can be considered. In addition, Equation (12) shows an anisotropy in the hydraulic conductivity tensor. It indicates that hydraulic conductivity in horizontal directions is greater than in vertical directions. This characteristic is observed and documented in the literature [31, pp. 100-103]. He states that K_x/K_z, with K_x and K_z respectively horizontal and vertical hydraulic conductivity, usually fall in the range 2 to 10 for alluvium, but values up to 100 or mode occur where clay layers are present.

Consider that $0 \leq \delta < 1$ and multiply 29 by $\frac{DU^2}{L}$ gives the Saint-Venant

system with ground influence in its dimensional form:

$$\begin{cases} \partial_t [h] + \partial_x [hu_f] + \partial_y [hv_f] = I \\ \partial_t [hu_f] + \partial_x \left[hu_f^2 + g\dfrac{h^2}{2} \right] + \partial_y [hu_f v_f] \\ \qquad = -k(u_f, v_f)u_f + \dfrac{\alpha_{\mathrm{BJ}}}{\sqrt{k_x + k_y}}(u_f - u_g) + Iu_f - gh\partial_x [z_b] \\ \partial_t [hv_f] + \partial_x [hu_f v_f] + \partial_y \left[hv_f^2 + g\dfrac{h^2}{2} \right] \\ \qquad = -k(u_f, v_f)v_f + \dfrac{\alpha_{\mathrm{BJ}}}{\sqrt{k_x + k_y}}(v_f - v_g) + Iv_f - gh\partial_y [z_b] \end{cases} \tag{30}$$

with $I = -u_g\partial_x z_b - v_g\partial_y z_b + w_g$ the quantity of water that enters (I>0) or leaves (I<0) the fluid domain.

Finally the two way coupled model of SWE and RE is given with the following system of equations :

$$\begin{cases} \partial_t h + \mathrm{div}(\mathbf{q}) = I, & \text{in } \Omega_{\mathrm{swe}}, \\ \partial_t \mathbf{q} + \mathrm{div}\left(\dfrac{\mathbf{q} \otimes \mathbf{q}}{h} + g\dfrac{h^2}{2}\mathbb{I} \right) = -k(\mathbf{u}_f)\mathbf{u}_f + \dfrac{\alpha_{\mathrm{BJ}}}{\sqrt{k_x + k_y}}(\mathbf{u}_f - \mathbf{u}_g) + I\mathbf{u}_f - gh\nabla z_b, & \text{in } \Omega_{\mathrm{swe}}, \\ I = \mathbf{u}_g \cdot (-\partial_x z_b, -\partial_y z_b, 1)^T, & \text{in } \Omega_{\mathrm{swe}}, \\ \mathbf{u}_g = -\mathbb{K}(\psi_g)\nabla h_g, & \text{in } \Omega_g, \\ \partial_t \theta(\psi_g) + \mathrm{div}(\mathbf{u}_g) = 0, & \text{in } \Omega_g, \\ h_g = h + z_b, & \text{on } \Gamma_C, \\ h_g = h_D, & \text{on } \Gamma_D, \\ -\mathbf{u}_g \cdot \mathbf{n} = q_N, & \text{on } \Gamma_N. \end{cases} \tag{31}$$

Unknowns of the problem are $(h, \mathbf{q}, h_g)$ respectively, the water height, the horizontal discharge, and the hydraulic head. Horizontal discharge is defined as $\mathbf{q} = (q_x, q_y)^T = \mathbf{u}_f h$ with $\mathbf{u}_f = (u_f, v_f)^T$ the horizontal velocity of the free-surface fluid. Moreover, z_b is the bottom topography, $\mathbb{K}$ is the hydraulic conductivity tensor, ψ_g is the hydraulic head, and θ is the water content. Constitutive laws for the ground domain are given in [9]. Several domains appear in System (31). It is important to notice that since SWE is obtained by vertically averaging Navier-Stokes equations, its definition domain is one dimension smaller than RE one. For instance, if $\Omega_g \subset \mathbb{R}^d$ then $\Omega_{\mathrm{swe}} \subset \mathbb{R}^{d-1}$ with $d = 2, 3$. First, the interface between the fluid and ground domains must be defined to define them properly. This interface is defined as Γ_C, which is the topography's graph. The domain Ω_{swe} is the SWE domain which is the orthonormal projection of Γ_C on the Oxy-plane. The domain Ω_g is the ground domain under the topography such that $\Gamma_C \subset \partial\Omega_g$. The remaining part of $\partial\Omega_g$ is split into two parts: Γ_D and Γ_N, respectively, the Dirichlet and Neumann boundary conditions. It is important to notice that Ω_{swe} is the reference plane fixing the origin for both SWE and RE.

Figure 1 shows the two domains Ω_{swe} and Ω_g with the interface Γ_C for the two-way coupled model in the two-dimensional case. Γ_C is depicted in dark sand color, Ω_g is the volume in light sand color and Ω_{swe} is the Oxy-plane in light

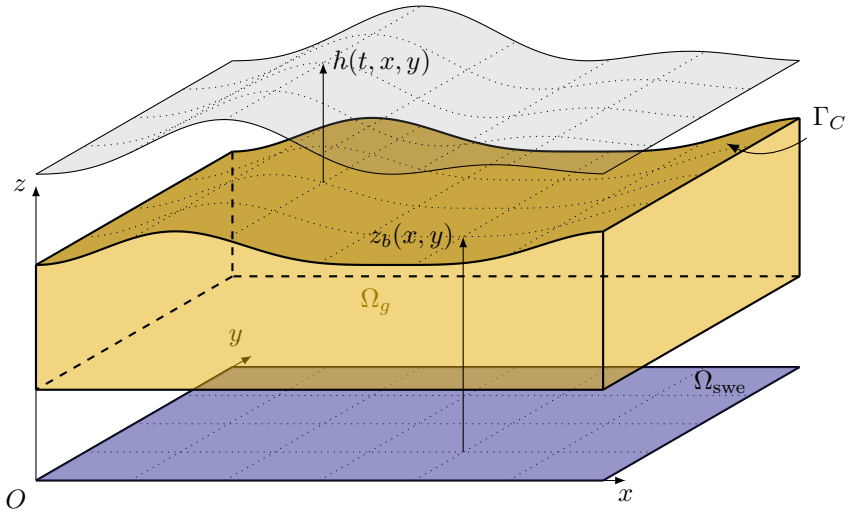

Figure 1: Representation of the two domain Ω_{swe} and Ω_g with the interface Γ_C for the two way coupled model.

blue. For the one-dimensional case, one may consider a vertical cross-section on Figure 1.

3 Numerical considerations of coupling RE and SWE

The preceding section derived a coupled model of RE and SWE equations. This model represents a two-way coupling of two models that encompass different physical processes. The (formal) justification of this coupled model has been established, although it does have limitations in its range of validity, whereas the one-way coupling is always valid. In the upcoming sections, we will consider the two-way coupling even when the problem is beyond its scope. This is justifiable as, outside of its scope, the interaction of the ground flow is, often, negligible compared to the surface flow. Before delving into how the coupled model is solved, an overview of different coupling methods is provided. For a comprehensive review of modeling coupled surface-sub-surface flows processes, readers can refer to [18], which presents coupling methods, coupled models with references, and the names of commercial software that solve such coupled problems.

3.1 Coupling methods

In the context of coupling surface and sub-surface models, it is crucial to properly define the coupling problem. Let's consider a global problem solved on a domain Ω, which can be divided into two subdomains Ω_1 and Ω_2, each with distinct physics. Also, let $L_1(u_1) = f_1$ and $L_2(u_2) = f_2$ denote the respective problems on Ω_1 and Ω_2, where u_i is the solution of problem i. It's important to note that the model on Ω_1 may not be valid on Ω_2 and vice versa. As a result, the two domains should not overlap but should share a common interface de-

noted Γ_C. The coupling constraint comes into play at this common edge, such as $u_1 = u_2$. If their respective solutions are incompatible, an operator $A_{1,2}$ is introduced, where $u_1 = A_{1,2}u_2$ and vice versa. This occurs when the two models do not have the same unknowns or the same space dimensions.

Three different levels of coupling between surface and sub-surface processes can be distinguished. Figure 2 depicts a scheme of these three methods. They include the one-way coupling (I, Ia), the two-way (iterative) coupling (II), and the full coupling. All three components are described in the following. In theory, the higher is the level of coupling, the higher is the accuracy.

The first level of numerical coupling is known as *one-way coupling*. In this approach, each system is independently solved at every time step, with the surface water component typically being solved first due to its faster dynamics. After obtaining the solution, an internal boundary condition value is specified, and then the other system is solved. There is no feedback loop used to correct the first system. An approximation is required because the boundary condition at the interface between the systems generally applies to both systems. It is convenient to use conditions from the previous time step to estimate the boundary conditions of the system that is solved first. This level of coupling is studied by Morita and Yen [23]. Clément *et al.* [7] employs this coupling level in the context of coupling RE and SWE.

The first level of coupling can be divided into two subcategories, the first of which has been explained previously. The second category involves representing one of the interacting systems (either surface or sub-surface) through an algebraic formulation (generally a specific solution for one of the systems). This approach is widely used by surface irrigation modelers and is referred to as degenerated uncoupled. Delestre adopts this level of coupling [11] with the Green and Ampt model for sub-surface flow.

The second level of coupling, *iterative coupling*, there is a feedback loop between the two systems. The initial steps are akin to those at the uncoupled level: the first system is solved, interfacial boundary conditions are defined, and the second system is solved using these boundary conditions. The difference lies in using the solution of the second system to update the internal boundary condition within the same time step. The first system is then solved again using this updated boundary condition, and this process is repeated until convergence criteria are met (typically until there is no significant change in one of the solved components). Morita and Yen [23] referred to this coupling level as *alternating iterative*. When there is only one iteration without seeking convergence, this coupling level is known as *parallel coupling*. In this approach, the two models are solved separately with their respective time steps, while the interface conditions (source terms) evolve according to the updated results. This type of coupling involves feedback but is always shifted in a kind of interlacing.

The third coupling level, which is the most complete, involves solving the two systems and the internal boundary conditions together. That is, the two PDEs and the interface equation (which may be an ordinary differential equation) are solved simultaneously. This coupling level is referred to here as *fully coupled*.

In this work, and the case of coupling RE and SWE the *parallel coupling* is chosen for its simplicity of implementation and its efficiency. Moreover, since the time steps for the surface flows are considerably smaller than the ground ones, the shifting between the two models is small.

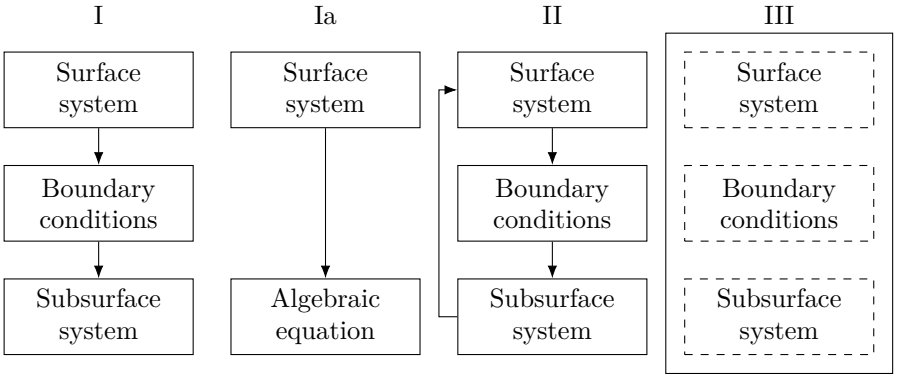

Figure 2: Different levels of coupling between surface and sub-surface processes.

3.2 Space synchronization

Because the SWE are obtained by averaging the Navier-Stokes equations along the vertical axis, there is a difference of one dimension between RE and SWE. It is common in the field of Computational Fluid Dynamics to couple models with different dimensional domains. For example, the Euler Bi-fluid equations are coupled with SWE (or Serre-Green-Naghdi Equations) [25], and the Navier-Stokes Equations are coupled with SWE [26]. In these cases, the averaging direction occurs along the interface between the two models. As a result, the coupling is achieved in both models using a boundary condition. However, in the case of RE and SWE, the averaging direction is perpendicular to the interface between the two models, leading to the coupling being achieved through a source term in SWE and a boundary condition in RE, with both equations being solved on separate domains.

First, let's define $\Omega_{\text{RE}} \subset \mathbb{R}^d$ as the domain for the RE model, where $d = 2$ or 3 represents the space dimension. Then, let's define $\Omega_{\text{SWE}} \subset \mathbb{R}^{d-1}$ as the domain for the SWE model. The boundaries of Ω_{RE} are divided into three subdomains: Γ_D, Γ_N, and Γ_C, corresponding to Dirichlet, Neumann, and Coupling boundary conditions, respectively. The coupling boundary Γ_C facilitates the exchange of information between the two models. In the case of the SWE model, information is obtained from the RE model through source terms, while for the RE model, information is received from the SWE model through boundary conditions on the coupling edge of the domain. Consequently, this information needs to be computed based on the approximations of the solutions of the two models. This is because the shared edge aligns with the averaging direction of the SWE model. In our specific case, the common edge shared by the initial models is perpendicular to the averaging direction of the SWE model. This implies that the exchange of information occurs across the entire domain Ω_{swe} and the entire edge Γ_C.

Both Ω_{RE} and Ω_{SWE} are discretized with meshes denoted as $\mathcal{E}^n_{\text{RE}}$ and $\mathcal{E}^n_{\text{SWE}}$, where $n \in \mathbb{N}$ indicates the time sub-interval T^n. For $\mathcal{E}^n_{\text{RE}}$, the set of boundary faces is represented as $\mathcal{F}^\partial = \mathcal{F}^D \cup \mathcal{F}^C \cup \mathcal{F}^N$, where $\mathcal{F}^D = \mathcal{F}^\partial \cap \Gamma_D$, $\mathcal{F}^N = \mathcal{F}^\partial \cap \Gamma_N$, and $\mathcal{F}^C = \mathcal{F}^\partial \cap \Gamma_C$. The mesh and domain representation for the coupling of SWE and RE with $d = 2$ can be seen in Figure 3. Furthermore, the two meshes are designed such that the number of blocks in $\mathcal{E}^n_{\text{SWE}}$ corresponds

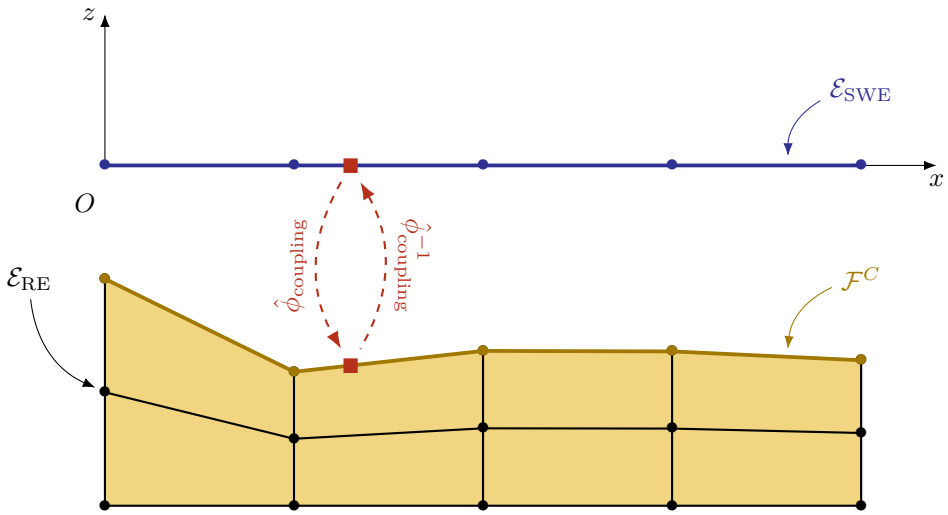

Figure 3: Mesh and domain representation for the coupling of SWE and RE.

to the number of blocks composing the coupling boundary of $\mathcal{E}^n_{\text{RE}}$. This design is not mandatory, but it helps the exchange of information between the two models and defines a coupling map function.

The resolution of SWE and RE with DG methods has been developed within the framework of adaptive mesh refinement [1] and [2]. Both models are solved on their respective meshes, which are composed of blocks that are refined at different levels. To facilitate the exchange of information, the aim is to have a conformal coupling interface. This means that each element E of $\mathcal{E}_{\text{SWE}}$ should correspond to a face of $\mathcal{F}^C$. Therefore, the refinement levels of the elements of $\mathcal{E}_{\text{SWE}}$ and the elements sharing a face with $\mathcal{F}^C$ need to be consistent.

Since the two meshes are distinct, to exchange information and compute the solution of RE in SWE and vice versa, a mapping function $\hat{\phi}_{\text{coupling}} : \Omega_{\text{SWE}} \to \Gamma_C$ is needed. This mapping function allows to evaluate the solution of RE on Ω_{SWE}, and its inverse allows to evaluate the solution of SWE on Γ_C. Recalling

$$\mathcal{V}^p(\mathcal{E}) := \left\{ v \in L^2(\Omega) \;\middle|\; v|_E \in \mathbb{P}^p(E),\ \forall E \in \mathcal{E} \right\}$$

where $\mathbb{P}^p(E)$ stands for the set of polynomial functions of degree less than or equal to $p \in \mathbb{N}$ on E (see [1, 2, 24] for further details) and using this mapping function and using DG space discretization weak formulations of System (31) is

(see [2] for further details):

Find $\mathbf{U} := (h, \mathbf{q})^T \in [\mathcal{V}^p(\mathcal{E}^n_{\text{SWE}})]^3$ such that $\forall t \in T^n,\ \forall E \in \mathcal{E}^n_{\text{SWE}}$ and $\forall \varphi \in [\mathcal{V}^p(\mathcal{E}^n_{\text{SWE}})]^3$,

$$\begin{cases} \displaystyle\sum_{E\in\mathcal{E}^n_{\text{SWE}}} \int_E \varphi(\mathbf{x})\partial_t \mathbf{U}(\mathbf{x},t)\mathrm{d}E - \sum_{E\in\mathcal{E}^n_{\text{SWE}}} \int_E \partial_{\mathbf{x}_i}\varphi(\mathbf{x})\mathbf{G}_i(\mathbf{U}(\mathbf{x},t))\mathrm{d}E \\ + \displaystyle\sum_{E\in\mathcal{E}^n_{\text{SWE}}} \sum_{F\in\mathcal{F}^E} \int_F \varphi(\mathbf{x})\mathbf{G}^*_F(\mathbf{U}(\mathbf{x},t))\mathrm{d}F = \sum_{E\in\mathcal{E}^n_{\text{SWE}}} \int_E \varphi(\mathbf{x})\mathbf{S}_b(\mathbf{U}(\mathbf{x},t),\tilde{z}_b(\mathbf{x}))\mathrm{d}E \\ + \displaystyle\sum_{E\in\mathcal{E}^n_{\text{SWE}}} \int_E \varphi(\mathbf{x})\mathbf{S}_f(\mathbf{U}(\mathbf{x},t))\mathrm{d}E + \sum_{E\in\mathcal{E}^n_{\text{SWE}}} \int_E \varphi(\mathbf{x})\mathbf{S}_{\text{RE}}(\mathbf{U}(\mathbf{x},t),\tilde{z}_b(\mathbf{x}),\mathbf{u}_g(\hat{\phi}_{\text{coupling}}(\mathbf{x})))\mathrm{d}E \end{cases} \tag{32}$$

where $\tilde{z}_b$ is the projection of the bathymetry onto $\mathcal{V}^p$ and $\mathbf{G}^*_F$ is the numerical flux (based on the Rusanov flux) across any face F. In addition, $\mathbf{S}_b$, $\mathbf{S}_f$ and $\mathbf{S}_{\text{RE}}$ are respectively the source terms due to bathymetry, friction and RE. The source term due to RE is computed using the map function ($\hat{\phi}_{\text{coupling}}$) between Ω_{swe} and Γ_C. And, for RE the weak formulation is (see [1] for further details):

Find $h \in \mathcal{V}^p(\mathcal{E}^n_{\text{RE}})$ such that $\forall t \in T^n,\ \forall E \in \mathcal{E}^n_{\text{RE}}$ and $\forall \varphi \in \mathcal{V}^p(\mathcal{E}^n_{\text{RE}})$,

$$\begin{cases} \displaystyle\sum_{E\in\mathcal{E}^n_{\text{RE}}} \int_E \partial_t\theta(h-z)\varphi\mathrm{d}E + \sum_{E\in\mathcal{E}^n_{\text{RE}}} \int_E (\mathbb{K}(h-z)\nabla h)\cdot\nabla\varphi\mathrm{d}E \\ - \displaystyle\sum_{F\in\mathcal{F}^{\text{in}}_{\text{RE}}} \int_F \{\!\!\{(\mathbb{K}(h-z)\nabla h)\cdot\mathbf{n_F}\}\!\!\}[\![\varphi]\!]\mathrm{d}F - \sum_{F\in\mathcal{F}^D_{\text{RE}}} \int_F (\mathbb{K}(h-z)\nabla h)\cdot\mathbf{n_F}\varphi\mathrm{d}F \\ + \displaystyle\sum_{F\in\mathcal{F}^{\text{in}}_{\text{RE}}} \frac{1}{2}\left(\frac{\sigma^{in}_E}{d_E} + \frac{\sigma^{in}_{E_r}}{d_{E_r}}\right) \int_F [\![h]\!][\![\varphi]\!]\mathrm{d}F + \sum_{F\in\mathcal{F}^C_{\text{RE}}} \frac{\sigma^{\partial}_E}{d_E}\int_F h\varphi\mathrm{d}F + \sum_{F\in\mathcal{F}^D_{\text{RE}}} \frac{\sigma^{\partial}_E}{d_E}\int_F h\varphi\mathrm{d}F \\ = \displaystyle\sum_{F\in\mathcal{F}^C_{\text{RE}}} \frac{\sigma^{\partial}_E}{d_E}\int_F (h+z_b)(\hat{\phi}^{-1}_{\text{coupling}}(\mathbf{x}))\varphi\mathrm{d}F + \sum_{F\in\mathcal{F}^D_{\text{RE}}} \frac{\sigma^{\partial}_E}{d_E}\int_F h_D\varphi\mathrm{d}F - \sum_{F\in\mathcal{F}^N_{\text{RE}}}\int_F q_N\varphi\mathrm{d}F \end{cases} \tag{33}$$

where $\mathbf{n_F}$, E_r, σ^{∂}_E, σ^{in}_E, d_E, $[\![v]\!]$ and $\{\!\!\{v\}\!\!\}$ are respectively, a normal pointing from E to E_r, a neighboring element E_r such that $E \cap E_r = F$, a boundary penalty parameter, an interior penalty parameter, the diameter of an element E defined as the ratio between its surface and its perimeter, the jump and the average of a function v on a face $F \in \mathcal{F}$:

$$\forall \mathbf{x} \in F,\ [\![v]\!](\mathbf{x}) := v_r(\mathbf{x}) - v_l(\mathbf{x}) \text{ and } \{\!\!\{v\}\!\!\}(\mathbf{x}) := \frac{1}{2}\big(v_r(\mathbf{x}) + v_l(\mathbf{x})\big)$$

where

$$v_l(\mathbf{x}) := \lim_{\varepsilon\to 0^-} v(\mathbf{x}+\varepsilon\mathbf{n}_F) \text{ and } v_r(\mathbf{x}) := \lim_{\varepsilon\to 0^+} v(\mathbf{x}+\varepsilon\mathbf{n}_F),\ \forall \mathbf{x} \in F.$$

On any boundary faces $F \in \mathcal{F}^{\partial}$ the trace of v is only defined on the left side of the face:

$$v_l(\mathbf{x}) := \lim_{\varepsilon\to 0^-} v(\mathbf{x}+\varepsilon\mathbf{n}_F),\ \forall \mathbf{x} \in F$$

and these quantities are defined by

$$\forall \mathbf{x} \in F,\ [\![v]\!](\mathbf{x}) := v_l(\mathbf{x}) \text{ and } \{\!\{v\}\!\}(\mathbf{x}) := v_l(\mathbf{x}).$$

In Problem (33), X_D and X_N stands for the Dirichlet and Neumann boundary condition on the generic variable X.

A variation exists on the boundary condition for the coupling term for RE. For now, the coupling is done using a Dirichlet boundary condition. It is well suited for problems that do not involve dry areas. In other words, problems where the porous medium is always covered by water. In the case of dry areas, a part of the porous medium is exposed to the atmosphere and imposing a Dirichlet boundary condition is not suitable. As mentioned in [7, 8], the seepage boundary condition models the interaction between the porous medium and the atmosphere. As a recall, the seepage boundary condition states that at the face exposed to the atmosphere, if an outflow occurs, then water pours out at atmospheric pressure, and otherwise, the porous medium acts as an impervious boundary; there is no flux. To implement this boundary condition, the coupling term in Problem (33) is modified as follows:

Find $h \in \mathcal{V}^p(\mathcal{E}^n_{\mathrm{RE}})$ such that $\forall t \in T^n,\ \forall E \in \mathcal{E}^n_{\mathrm{RE}}$ and $\forall \varphi \in \mathcal{V}^p(\mathcal{E}^n_{\mathrm{RE}})$,

$$\begin{cases} \displaystyle\sum_{E\in\mathcal{E}^n_{\mathrm{RE}}} \int_E \partial_t\theta(h-z)\varphi \mathrm{d}E + \sum_{E\in\mathcal{E}^n_{\mathrm{RE}}} \int_E (\mathbb{K}(h-z)\nabla h)\cdot\nabla\varphi \mathrm{d}E \\ \displaystyle - \sum_{F\in\mathcal{F}^{\mathrm{in}}_{\mathrm{RE}}} \int_F \{\!\{(\mathbb{K}(h-z)\nabla h)\cdot\mathbf{n_F}\}\!\}[\![\varphi]\!]\mathrm{d}F - \sum_{F\in\mathcal{F}^D_{\mathrm{RE}}} \int_F (\mathbb{K}(h-z)\nabla h)\cdot\mathbf{n_F}\varphi \mathrm{d}F \\ \displaystyle + \sum_{F\in\mathcal{F}^{\mathrm{in}}_{\mathrm{RE}}} \frac{1}{2}\left(\frac{\sigma^{in}_E}{d_E} + \frac{\sigma^{in}_{E_r}}{d_{E_r}}\right)\int_F [\![h]\!][\![\varphi]\!]\mathrm{d}F + \sum_{F\in\mathcal{F}^C_{\mathrm{RE}}} \frac{\sigma^{\partial}_E}{d_E}\int_F \mathbb{1}_{SC}(\mathbf{x})h\varphi \mathrm{d}F + \sum_{F\in\mathcal{F}^D_{\mathrm{RE}}} \frac{\sigma^{\partial}_E}{d_E}\int_F h\varphi \mathrm{d}F \\ \displaystyle = \sum_{F\in\mathcal{F}^C_{\mathrm{RE}}} \frac{\sigma^{\partial}_E}{d_E}\int_F \mathbb{1}_{SC}(\mathbf{x})(h+z_b)(\hat{\phi}^{-1}_{\mathrm{coupling}}(\mathbf{x}))\varphi \mathrm{d}F + \sum_{F\in\mathcal{F}^D_{\mathrm{RE}}} \frac{\sigma^{\partial}_E}{d_E}\int_F h_D\varphi \mathrm{d}F - \sum_{F\in\mathcal{F}^N_{\mathrm{RE}}}\int_F q_N\varphi \mathrm{d}F \end{cases} \tag{34}$$

with $\mathbb{1}_{SC}$ the indicator function of the coupling seepage boundary condition. This function is defined as follows:

$$\mathbb{1}_{SC}(\mathbf{x}) = \begin{cases} 1 \text{ if } h(\hat{\phi}^{-1}_{\mathrm{coupling}}(\mathbf{x})) > 0 \text{ or } h_g(\mathbf{x}) \geq z \\ 0 \text{ otherwise} \end{cases} \tag{35}$$

One can see that in the case of a fully wet problem Problem (34) and Problem (33) are equivalent, but in the case of dry areas the coupling seepage boundary condition becomes a classical seepage boundary condition.

Weak formulation of Problem (32) and Problem (34) are used to compute an approximated solution of the two-way coupling problem. Nevertheless, these weak formulations are still semi-discrete. Time integration needs to be performed to have fully discretized problems.

3.3 Time synchronization

Typically, surface and groundwater flows have different time scales. In particular, for most surface water flows, the time steps needed for stability and accuracy

of numerical methods are seconds to minutes. For groundwater flow, time steps are generally from minutes to days. Consider that for the groundwater flows problem, its computational time is discretized with sub-intervals $T^n := [t^n, t^{n+1}]$ with $\Delta t^n_{\text{RE}} := t^{n+1} - t^n$. Now each sub-interval T^n is split into K sub-intervals with for all $k = 1, \ldots, K$ $T^{n,k} := [t^{n,k}, t^{n,k+1}]$ with $\Delta t^{n,k}_{\text{SWE}} := t^{n,k+1} - t^{n,k}$ and by definition $t^{n,1} := t^n$ and $t^{n,K+1} := t^{n+1}$. As seen in [1] and [2] the semi-discrete weak formulation of RE is time-integrated using an implicit method on T^n whereas the semi-discrete weak formulation of SWE is time-integrated using an explicit method on each $T^{n,k}$. The time synchronization procedure is depicted in Figure 4 with Roman figures enumerating the different stages. It is composed of four main steps:

[I] This is the first exchange of information between the two models. They exchange their respective solution at the time t^n. The solution is exchanged under its algebraic representation, and degrees of freedom are exchanged for memory consumption and efficiency. Since the solutions exchanged live in their respective solution space, the mapping function is useful for evaluating the solution of RE on Ω_{SWE}, and its inverse allows evaluating the solution of SWE on Γ_C.

[II] RE is solved on T^n using the implicit Backward Differentiation Formula (BDF) method. The solution of SWE at t^n is used in the boundary condition. The non-linear iterative solver presented [1] with adaptive time stepping is used, and the next step of the time synchronization is performed only when the converged solution at t^{n+1} is obtained.

[III] This is the second exchange of information between the two models. The solution of RE at t^{n+1} is exchanged to SWE following the same procedure as [I].

[IV] SWE is solved on $T^{n,k}$ for all $k = 1, \ldots, K$ using the explicit Runge-Kutta Discontinuous Galerkin (RKDG) method. In the source terms of SWE the solution of RE is linearly interpolated in time using the solution of RE at t^n and t^{n+1}. The well-balanced property, the limiting procedure, and the flooding and drying treatment are performed as explained in [2]. Time steps of SWE are computed through a Courant-Friedrichs-Lewy (CFL) condition. Thus they are not constant and may vary from one time step to another.

One can observe that the groundwater flow is shifted backward in time since it uses the surface flow solution at t^n to compute the solution at t^{n+1}. The benefit of this method is that the slowest problem pilots the global time stepping and consequently the amount of shift. There exists a variation in the time synchronization strategy. One can first solve SWE with the solution of RE at t^n in source terms and then solve RE with the solution of SWE at t^{n+1} in the boundary condition. This way, the shift between the two models is displaced from RE to SWE but it is observed that the solution is not significantly impacted by this method.

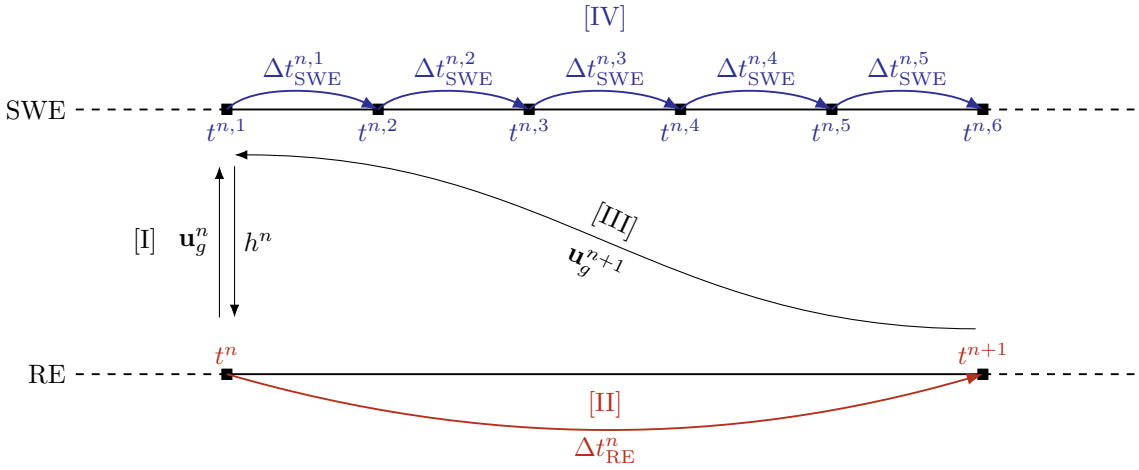

Figure 4: Scheme of time synchronization between RE and SWE for T^n with $K = 5$.

4 Numerical toy problem end experimental benchmark for validation

The coupling methodology described before and DG methods introduced in [1, 2] is implemented in `RIVAGE`. It leads to an in-house code that solves problems involving computing interactions between free-surface and groundwater flows. These newly implemented methods need to be validated. Because it is new to couple these two models, there are few benchmarks to validate `RIVAGE`. In this section, firstly, a toy problem is considered to test if the expected phenomenon of a coupled problem is presented; this is a qualitative validation. Secondly, an experimental benchmark is considered to validate the code; this is a quantitative validation.

4.1 Coupled groundwater and free-surface flow: toy problem

The first test case is a toy problem. It is a simple test case assessing the coupling between the groundwater and free-surface flows. The free-surface domain considered is a one-dimensional domain with a flat bathymetry. The groundwater domain is a two-dimensional rectangular domain. A traveling wave over the ground domain is considered, and water can flow through it. During this considered problem, several phenomena are expected to be observed:

- The wave should travel freely over the ground domain;
- Hydraulic head distribution should be modified by the traveling wave;
- The global water level should decrease due to infiltration in the ground domain.

Figure 5 depicts the toy problem's configuration. The ground domain (Ω_g) is a 20×5 m box with impervious sides ($q_N = 0$ $m.s^{-1}$) and hydraulic head imposed

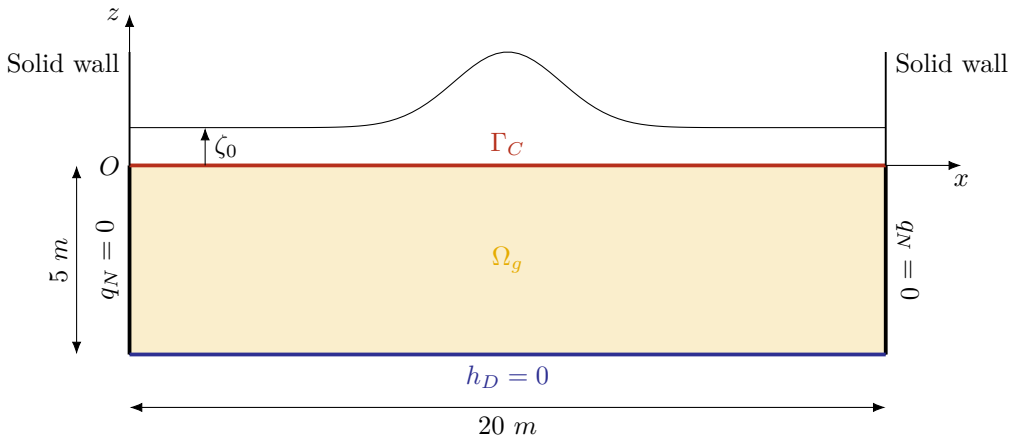

Figure 5: Coupling toy problem's configuration

on the bottom ($h_D = -1\ m$). The box is full of sand, saturated with water. Hydraulic properties use Vachaud's relations in [7] with $A = 2.99\,10^6$, $B = 5.0$, $C = 40000, D = 2.9, Ks = 9.72\,10^{-2}\ m.s^{-1}, \theta_s = 0.3$ and $\theta_r = 0.0$. The fluid domain (Ω_f) is a $20m$ long canal with flat bathymetry and solid walls at the ends. The two domains are linked through Γ_C. No friction is considered on the bottom of the fluid domain, hence $C_{\text{tur}} = C_{\text{lam}} = 0$ and $\alpha_{\text{BJ}} = 0$.Initial data are given by:

$$\forall \mathbf{x} \in \Omega_g,\ h_g(\mathbf{x}, 0) = 0.4y + 1 \text{ and } \forall \mathbf{x} \in \Omega_f,\ \zeta(\mathbf{x}, 0) = 1 + 2e^{-x^2}.$$

The problem is solved using DG methods, seeking solutions in $\mathcal{V}^1$ with BDF and Runge-Kutta (RK) integration methods of order 2. Block Based Adaptive Mesh Refinement (BB-AMR) techniques are used for both SWE and RE. For the fluid domain, the adaptation criterion is based on the gradient of the water height with $\beta_c = \beta_r = 0.025$ (see [2] for instance). For the ground domain, the adaptation criterion is based on the gradient of the hydraulic head with $\beta_c = \beta_r = 0.2$. The initial mesh is given in Figure 6. The simulation is carried out until $T = 20\ s$. Auto calibration of penalization parameters is used, and moment limiters are set to the least diffusive for the SWE. The non-linear solver's stopping criteria are set to $\varepsilon_1 = \varepsilon_2 = 10^{-6}$.

Figures 7 to 9 display the solution of the toy problem at selected times. The hydraulic head distribution is shown in color grading, the free surface elevation is black, the initial free surface elevation is red, and the mesh is white. The figures show the expected phenomenon of the toy problem. The wave travels freely over the ground domain, and its momentum is diminished due to friction related to infiltration. The wave modifies the hydraulic head distribution, and the global water level decreases due to infiltration in the ground domain. The numerical results are in agreement with the expected phenomenon. Moreover, the Adaptive Mesh Refinement (AMR) technique follows phenomena. The mesh is refined where the wave is located and where the hydraulic head distribution is modified. The mesh is coarsened where the gradient is low and where the wave has already passed.

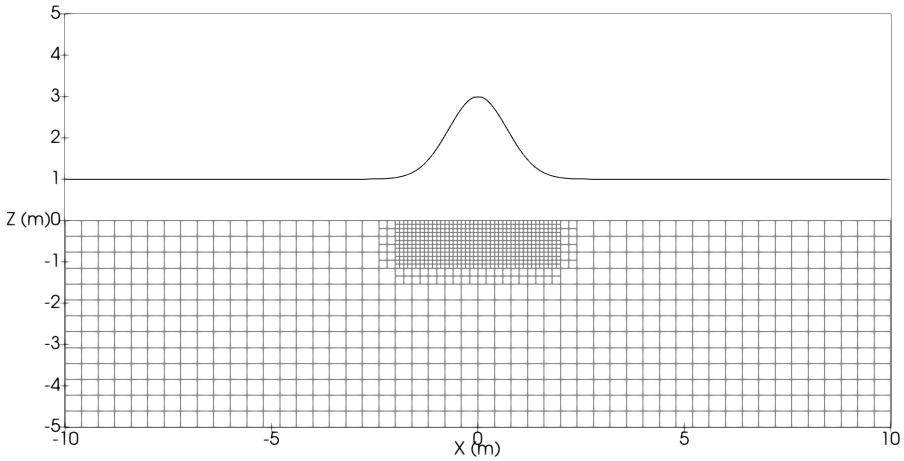

Figure 6: Coupling toy problem's initial mesh

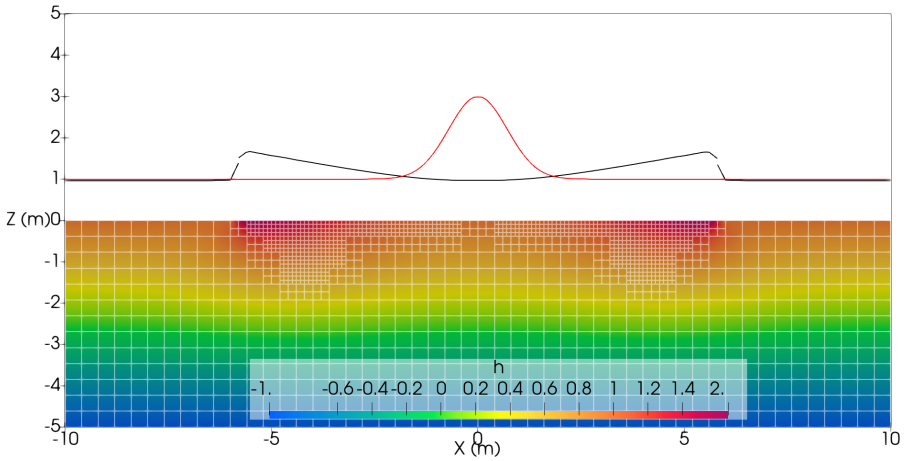

Figure 7: Coupling toy problem's hydraulic head distribution (color grading), free surface elevation (black line), initial free surface elevation (red line) and mesh (white lines) at $t = 1\ s$

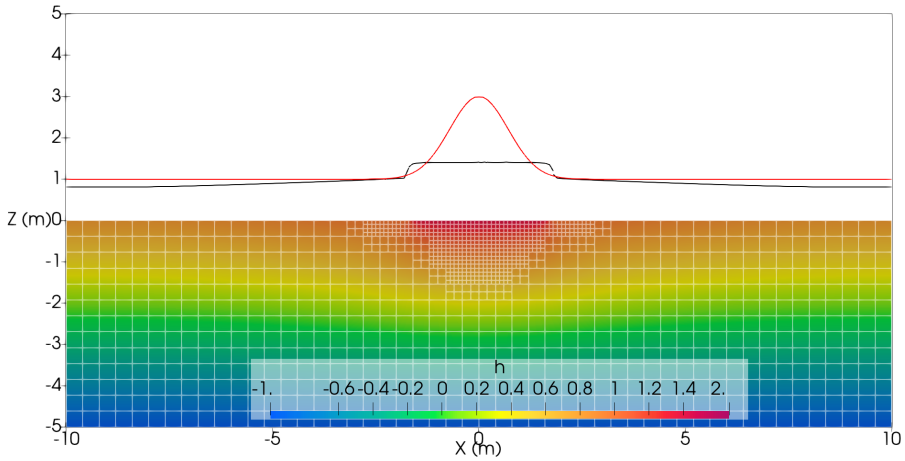

Figure 8: Coupling toy problem's hydraulic head distribution (color grading), free surface elevation (black line), initial free surface elevation (red line) and mesh (white lines) at $t = 5\ s$

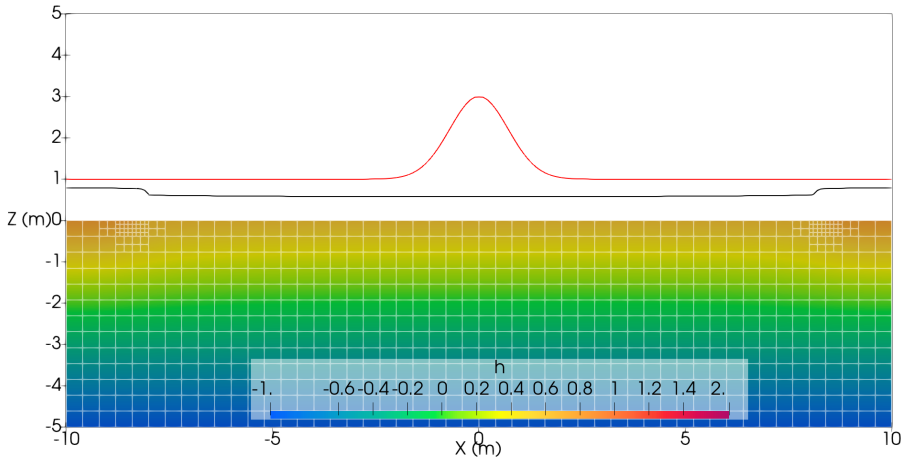

Figure 9: Coupling toy problem's hydraulic head distribution (color grading), free surface elevation (black line), initial free surface elevation (red line) and mesh (white lines) at $t = 15\ s$

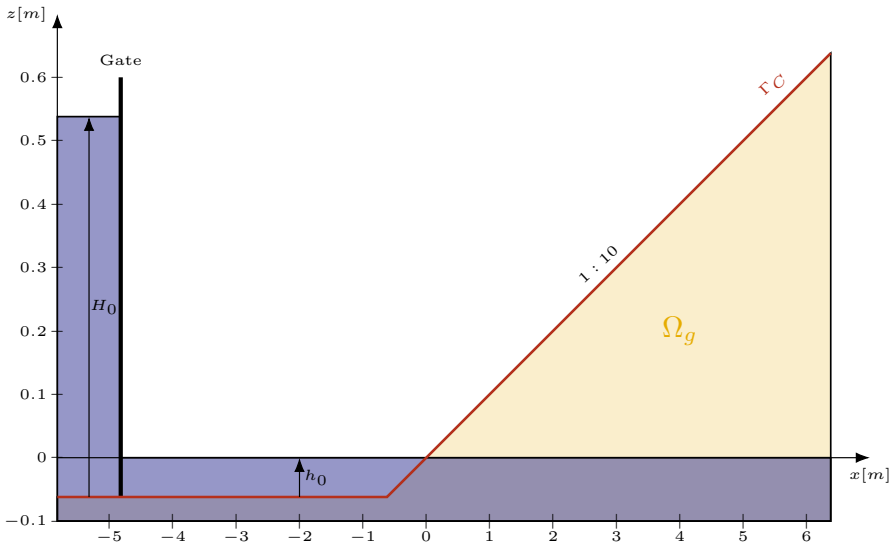

Figure 10: Steenhauer's test case configuration

4.2 Coupled groundwater and free-surface flow: Steenhauer's test case

Bore-driven swash on unsaturated coarse-grained beaches involves several interacting processes: surface flow over the beach face, infiltration into the unsaturated part of the beach, air entrapment below the wetting front, and groundwater flow. This phenomenon was observed during an experiment by Steenhauer *et al.* [30]. They used a 20 m long, 0.9 m high, and 0.45 m wide flume with a water reservoir at one end and a beach plane at the other end. A bore is generated by quickly raising the gate of the reservoir. The bore propagates to the beach, leading to a swash event typical of natural beaches. The beach is a $1:10$ slope located at 4 m downstream of the reservoir. Figure 10 depicts a cross-section of the reservoir, hence, the experiment's configuration. The beach is made of sediment throughout its depth, with the top 30 mm bonded by a diluted water-cement-sediment mix, maintaining the permeability and roughness but preventing the sediment from moving. This experiment involves two different materials: one with a nominal diameter of 1.5 mm (denoted $d_{1.5}$) and another with 8.5 mm (denoted $d_{8.5}$). Samples of the two sediments are shown in Figure 11. The porous media is characterized by Vachaud's law [7]. Physical parameters can be found in Table 1. Shape parameters of Vachaud's law are calibrated to have a classical shape of constitutive considering that the capillary fringe for $d_{8.5}$ is smaller than for $d_{1.5}$. Hydraulic conductivity is extracted from the literature [29] and anisotropy (with a ratio of 5) is considered. Saturated and residual water content are extracted for the literature [29]. Friction coefficients are set empirically to match the experimental results. Lastly, α_{BJ} is set to 0 because the time scales of the problem are too different from each other.

Figure 11: Steenhauer's test case sediments [30]

	A	**B**	**C**	**D**	$\mathbf{K_{s,x}}$	$\mathbf{K_{s,z}}$	$\theta_\mathbf{s}$	$\theta_\mathbf{r}$	$\mathbf{C}_{\text{lam}}$	$\mathbf{C}_{\text{tur}}$	α_{BJ}
unit	-	-	-	-	$m.s^{-1}$	$m.s^{-1}$	-	-	$m.s^{-1}$	-	-
$\mathbf{d_{1.5}}$	$5\,10^{-5}$	2.5	$5\,10^{-4}$	2.5	$1.27\,10^{-2}$	$2.54\,10^{-3}$	0.3	0.0	0.0	0.01	0
$\mathbf{d_{8.5}}$	$5\,10^{-5}$	2.0	$5\,10^{-4}$	2.0	$2.45\,10^{-1}$	$4.90\,10^{-2}$	0.3	0.0	0.0	0.02	0

Table 1: Steenhauer's test case, physical parameters

Initial water height (h) for the free-surface flow is given by:

$$\forall x \in \Omega_f,\ h(x,0) = \begin{cases} H_0\ m, & \text{if } x < -4.82\ m \\ h_0\ m, & \text{if } 4.82\ m \leq x < -0.62\ m \\ -x/10\ m, & \text{if } -0.62\ m \leq x < 0\ m \\ 0.0\ m, & \text{if } x \geq 0\ m \end{cases}$$

with $H_0 = 0.6\ m$ and $h_0 = 0.062\ m$. Initial hydraulic head (h_g) for the groundwater flow is given by:

$$\forall \mathbf{x} \in \Omega_g,\ h_g(\mathbf{x},0) = 0.0\ m.$$

Boundary conditions considered are for this test case are:

- Solid wall at both en of Ω_f;
- Impervious walls at left, right and bottom sides of Ω_g;
- Coupling boundary condition on Γ_C.

For both sediments, the problem is solved using DG methods, seeking solutions in $\mathcal{V}^1$ with BDF and RK integration methods of order 2 with $\alpha_{\text{CFL}} = 0.9$. The simulation is carried out until $T = 10\ s$. BB-AMR techniques are used for both SWE and RE. For the fluid domain, the adaptation criterion is based on the gradient of free surface elevation with $\beta_c = \beta_r = 0.01$ (see [2] for instance). In addition, if a block contains the shoreline, it is refined. For the ground domain, the adaptation criterion is based on the water content gradient with $\beta_c = \beta_r = 1.5$. The initial mesh is given in Figure 12. Auto calibration of penalization parameters and moment limiters, set to the least diffusive, are used for the SWE. For the wetting and drying treatment, slope modification

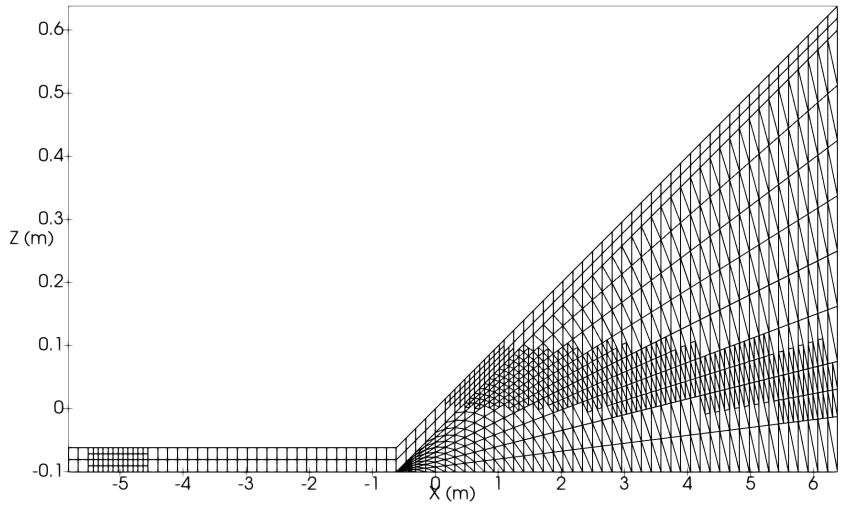

Figure 12: Steenhauer's test case initial mesh

is used with $h_{\text{dry}} = 10^{-3}$. The non-linear solver's stopping criteria are set to $\varepsilon_1 = \varepsilon_2 = 10^{-3}$. Time adaptation is used with $m_{it} = 10$, $M_{it} = 20$ and $W_{it} = 25$ (see [1]).

Results for $d_{1.5}$

Figures 13 to 16 depicts the computed solution for $d_{1.5}$ at selected times. The hydraulic head distribution is shown with color grading, the free surface elevation is black, the water table is white, and the mesh is black. One can observe that $t = 2.00$ s the bore reaches the beach with a height of 20 cm as expected and observed in the experiment [30]. At $t = 3.00$ s, the bore propagates over the beach, the hydraulic head distribution is modified, and water infiltrates the porous medium. At $t = 4.80$ s, the bore has reached its maximum covering of the beach and starts retreating, water is still infiltrating, and groundwater is moving through the sand. At $t = 7.00$ s, the bore retreats, and the water table follows the bore. Nevertheless, water still moves vertically after the bore covers the beach. One can see that during the whole run-up of the bore, air is trapped between water infiltrating from the wave and the water table. This phenomenon is observed in the experiment.

Figure 17 compares results extracted from the work of Steenhauer *et al.* in 2012 [29] with numerical results computed with `RIVAGE`. One can observe that the free surface elevation is well recovered; however, at $t = 5.11$ s, the maximum covering of the beach by the bore is underestimated. It may be caused by poor calibration of the friction coefficient. One can do several tests by trial and error to find the best value for the friction coefficient. One can see that the infiltration from the wave is well recovered in terms of the groundwater flow. However, in the literature, the connection between the initial water table and the infiltrating water table does not move, whereas, in our numerical results, it moves to the right.

During the experiments, gauges to record hydraulic head were placed at sev-

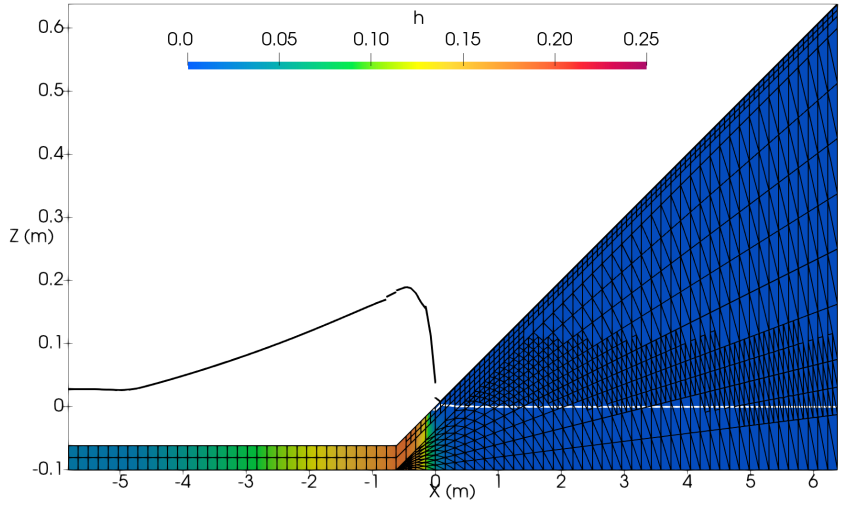

Figure 13: Steenhauer's test case, hydraulic head distribution (color grading), free surface elevation (black line), water table (white line) and mesh at $t = 2.00\ s$ for $d_{1.5}$

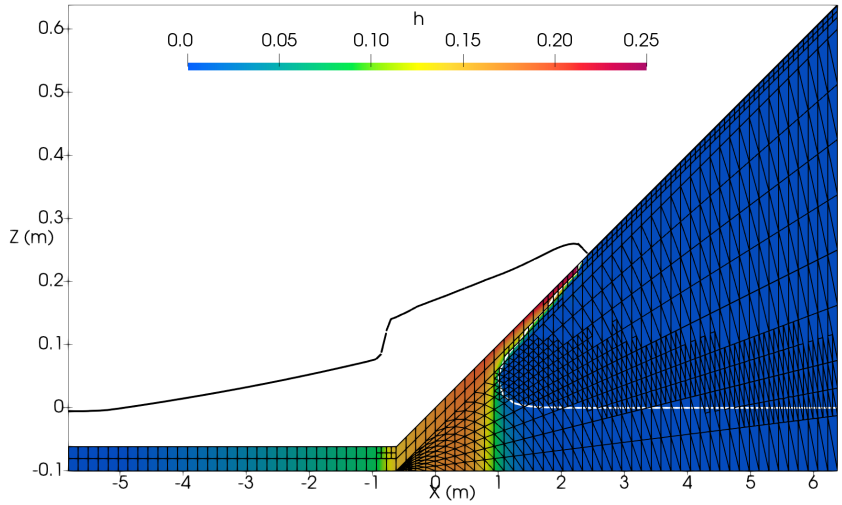

Figure 14: Steenhauer's test case, hydraulic head distribution (color grading), free surface elevation (black line), water table (white line) and mesh at $t = 3.00\ s$ for $d_{1.5}$

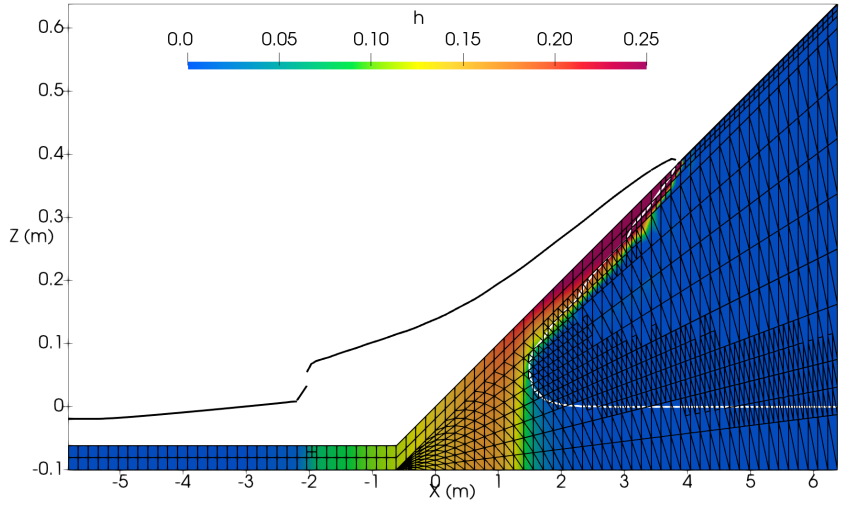

Figure 15: Steenhauer's test case, hydraulic head distribution (color grading), free surface elevation (black line), water table (white line) and mesh at $t = 4.80\ s$ for $d_{1.5}$

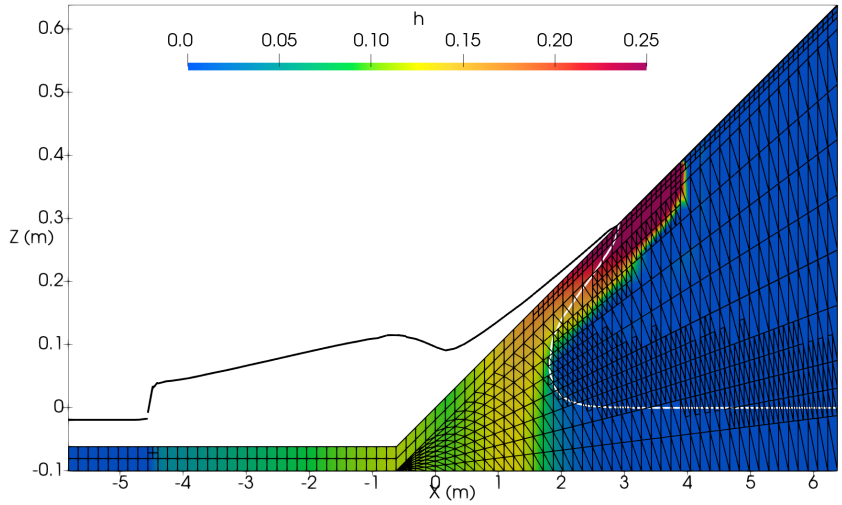

Figure 16: Steenhauer's test case, hydraulic head distribution (color grading), free surface elevation (black line), water table (white line) and mesh at $t = 7.00\ s$ for $d_{1.5}$

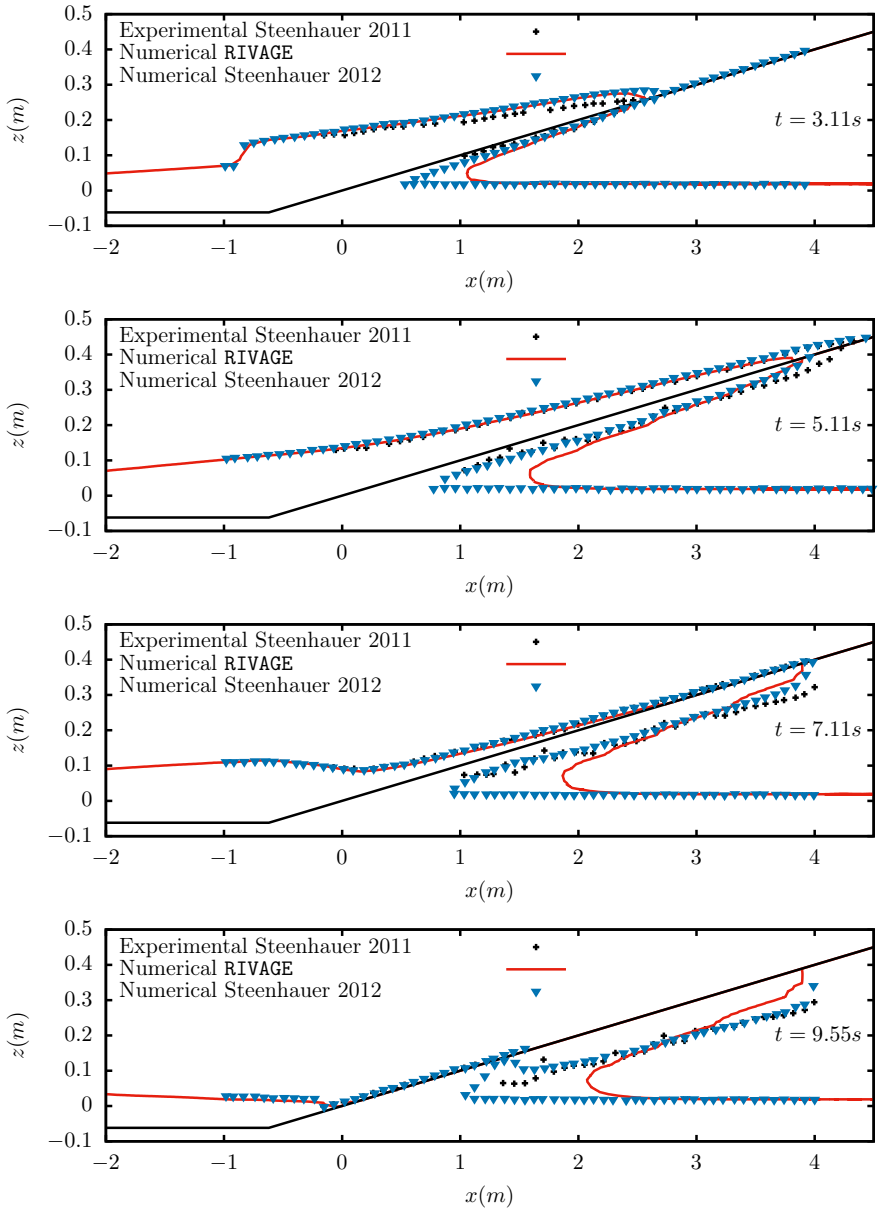

Figure 17: Steenhauer's test case, comparison of numerical results $\mathcal{V}^1$ (red line) with experimental results,[30] (black cross) and numerical results, [29] (blue triangle) for $d_{1.5}$

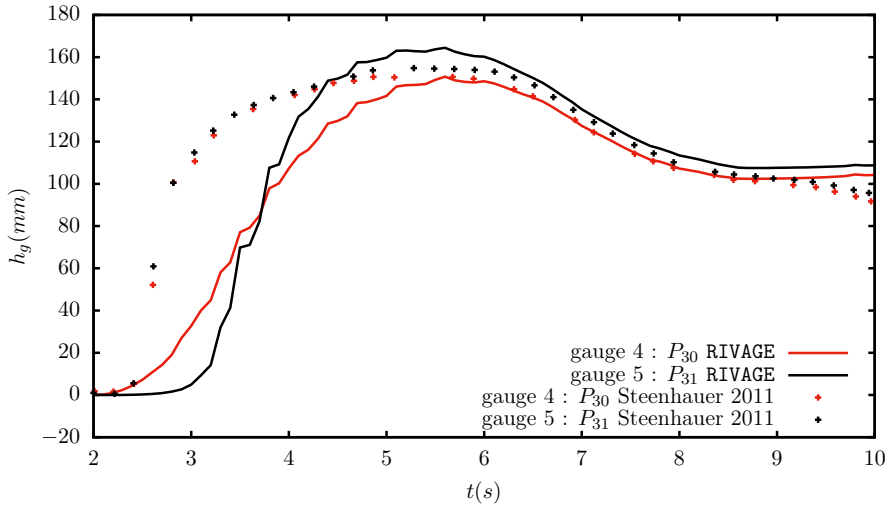

Figure 18: Steenhauer's test case, time series of the hydraulic head of numerical results $\mathcal{V}^1$ (solid lines) and experimental results, [30] (crosses) for gauges P_{30} and P_{31}

eral locations. Figure 18 depicts time series of hydraulic head of numerical results $\mathcal{V}^1$ and experimental results for gauges P_{30} and P_{31} placed at $x = 1180\ mm$ and respectively $y = -65.9\ mm$ and $y = -65.9\ mm$. One can see that the maximum hydraulic head value is well recovered. Nevertheless, the numerical results do not recover the overall shape of the time series. It may be due to the choice of constitutive law for the porous media and/or law parameters. There is a need to calibrate the constitutive law parameters to fit the experimental results better.

Figure 19 displays the evolution of time steps and the number of elements over time. The adaptation of time steps and the number of elements is evident. Time steps are maximum before the arrival of the bore to the beach ($t = 2\ s$). Then, during the whole run-up phase, time steps are reduced to catch strong non-linearities due to water infiltration from the free surface flow. Once the run-down phase begins, the time steps return to its maximum Δt_{amr}. The number of elements is evolving with time and the adaptation criteria. Evolution of the mesh can be observed in Figures 13 to 16.

Results for $d_{8.5}$

Figures 20 to 23 depicts the computed solution for $d_{1.5}$ at selected times. The hydraulic head distribution is shown with color grading, the free surface elevation is black, the water table is white and, the mesh is black. One can observe that $t = 2.00\ s$ the bore reaches the beach with a height of 20 cm as expected and observed in the experiment [30]. At $t = 3.00\ s$, the bore propagates over the beach, the hydraulic head distribution is modified, and water infiltrates the porous medium. At $t = 4.20\ s$, the bore has reached its maximum covering of the beach and starts retreating, water is still infiltrating, and groundwater is moving through the sand. At $t = 7.00\ s$, the bore retreats, and the water table

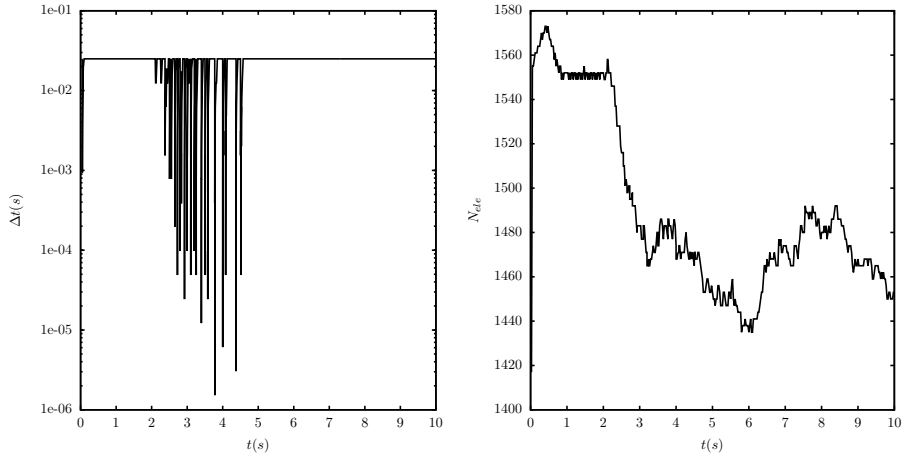

Figure 19: Steenhauer's test case, evolution along time of time steps (left) and number of elements (right)

follows the bore. Nevertheless, water still moves vertically after the bore covers the beach. One can see that during the whole run-up of the bore, in this case no air is trapped between water infiltrating from the wave and the water table. This phenomenon is observed in the experiment.

Figure 24 compares results extracted from the work of Steenhauer *et al.* in 2012 [29] with numerical results computed with `RIVAGE`. One can observe that the free surface elevation is well recovered. However, the maximum covering of the beach by the bore is underestimated. It may be caused by poor calibration of the friction coefficient. One can see that the infiltration from the wave is well recovered in terms of the groundwater flow. However, in literature, the connection between the initial water table and the infiltrating water table moves slower to the right than numerical results.

During the experiments, gauges to record hydraulic head were placed at several locations. Figure 25 depicts time series of hydraulic head of numerical results $\mathcal{V}^1$ and experimental results for gauges P_{30} and P_{40} placed respectively at $x = 1180\ mm$, $y = -67.8\ mm$ and $x = 1980\ mm$, $y = -65.1\ mm$. One can see that the maximum hydraulic head value is well recovered. Nevertheless, the numerical results do not recover the overall shape of the time series. It may be due to the choice of constitutive law for the porous media and/or law parameters.

Figure 26 displays the evolution of time steps and the number of elements over time. The adaptation of time steps and the number of elements is evident. Time steps are maximum before the arrival of the bore to the beach ($t = 2\ s$). Then, during the whole run-up phase, time steps are reduced to catch strong non-linearities due to water infiltration from the free surface flow. Once the run-down phase begins, the time steps return to its maximum Δt_{amr}. The number of elements is evolving with time and the adaptation criteria. Evolution of the mesh can be observed in Figures 20 to 23.

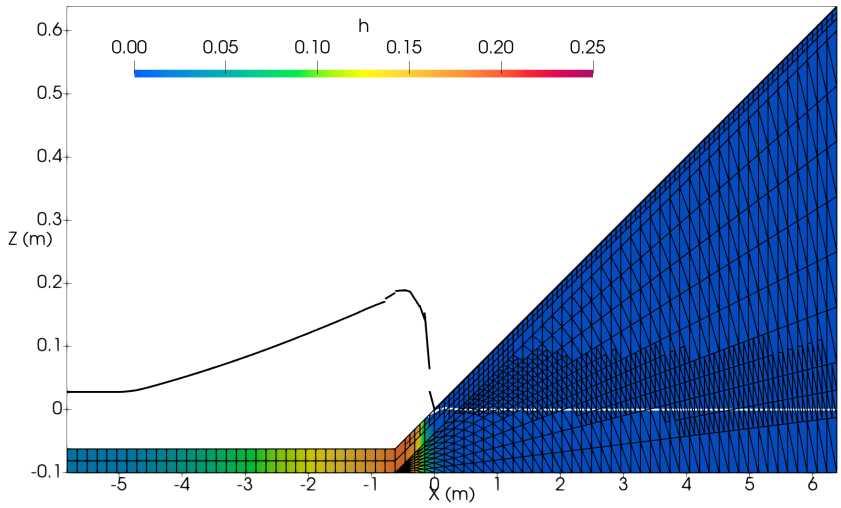

Figure 20: Steenhauer's test case, hydraulic head distribution (color grading), free surface elevation (black line), water table (white line) and mesh at $t = 2.00\ s$ for $d_{8.5}$

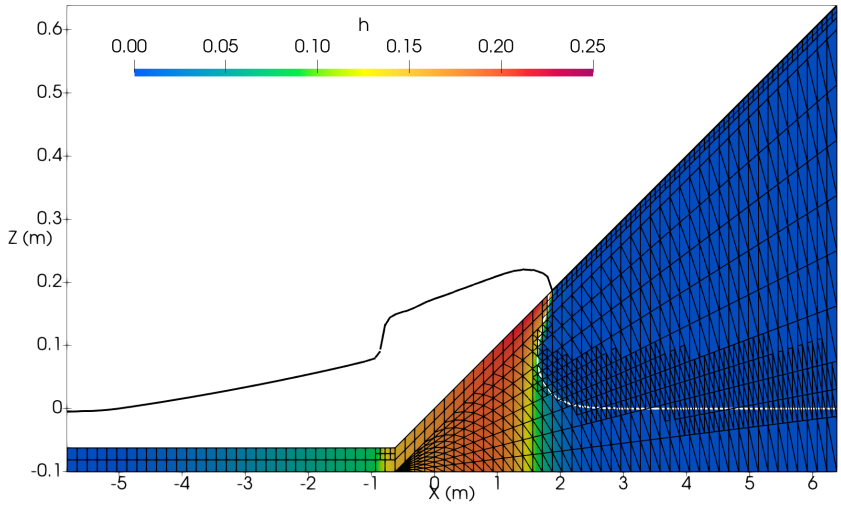

Figure 21: Steenhauer's test case, hydraulic head distribution (color grading), free surface elevation (black line), water table (white line) and mesh at $t = 3.00\ s$ for $d_{8.5}$

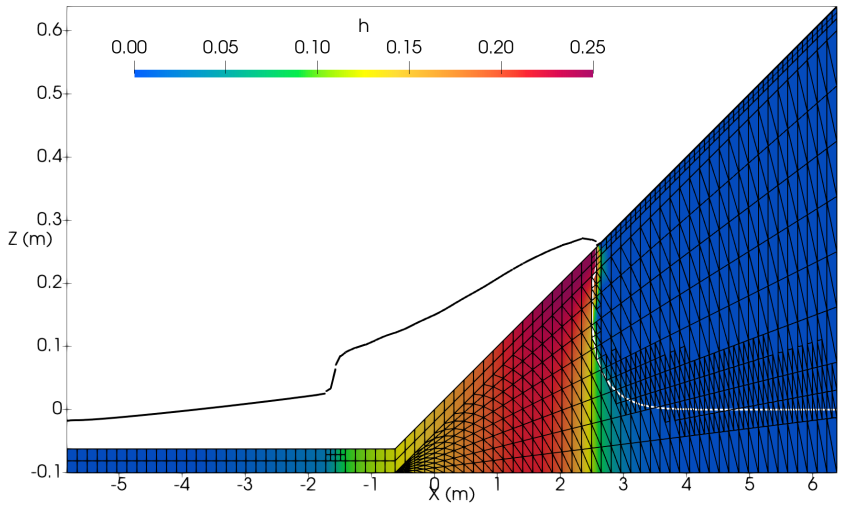

Figure 22: Steenhauer's test case, hydraulic head distribution (color grading), free surface elevation (black line), water table (white line) and mesh at $t = 4.20\ s$ for $d_{8.5}$

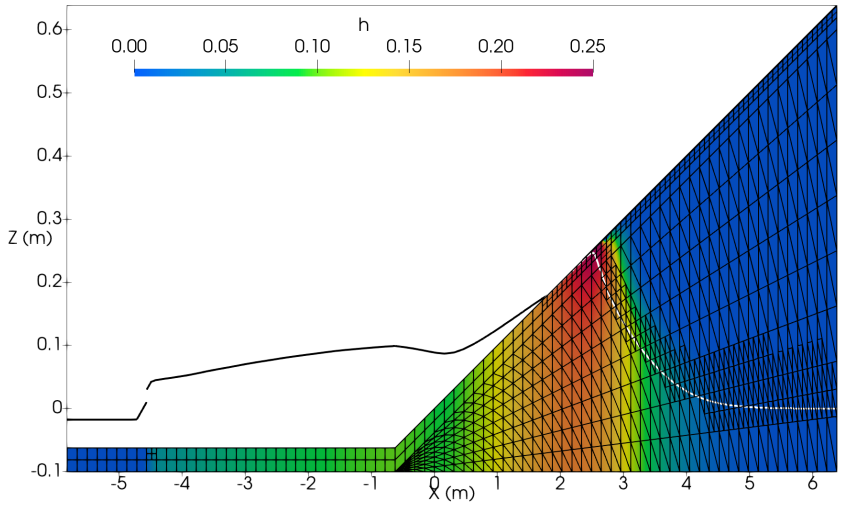

Figure 23: Steenhauer's test case, hydraulic head distribution (color grading), free surface elevation (black line), water table (white line) and mesh at $t = 7.00\ s$ for $d_{8.5}$

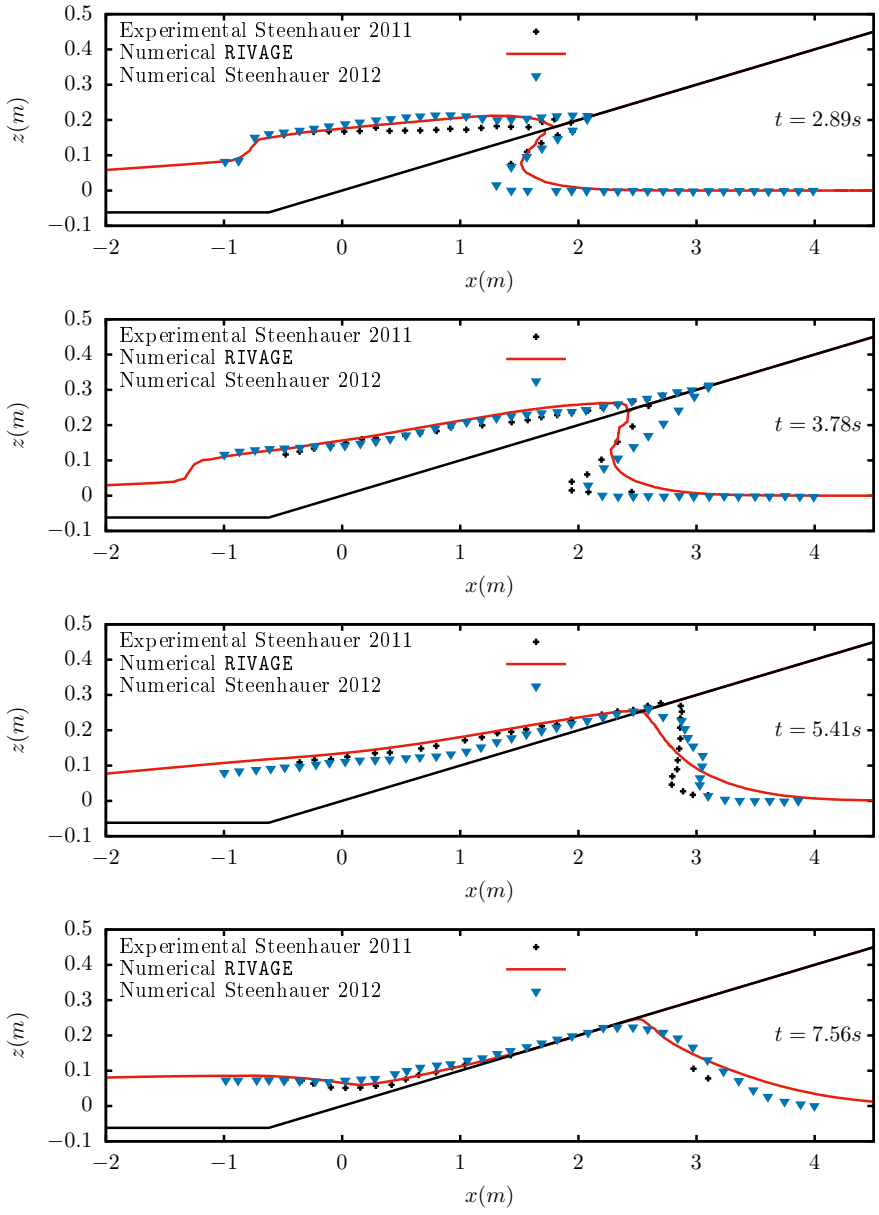

Figure 24: Steenhauer's test case, comparison of numerical results $\mathcal{V}^1$ (red line) with experimental results,[30] (black cross) and numerical results, [29] (blue triangle) for $d_{8.5}$

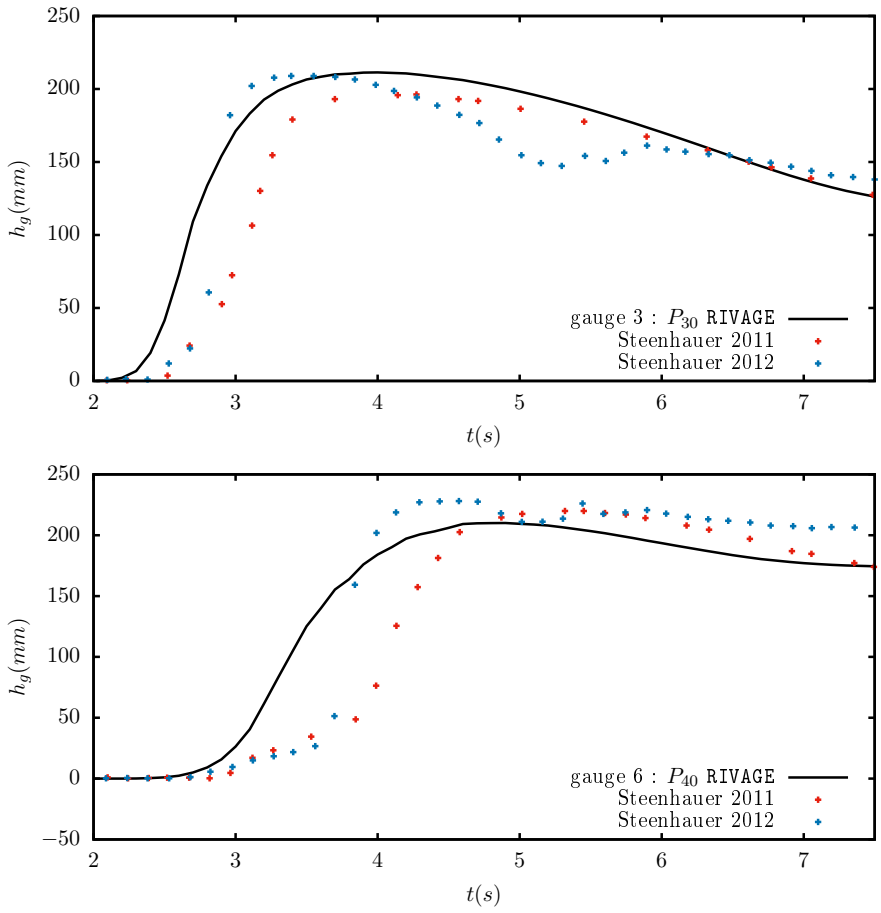

Figure 25: Steenhauer's test case, time series of the hydraulic head of numerical results $\mathcal{V}^1$ (solid lines) and experimental results, [30] (crosses) for gauges P_{30} and P_{31}

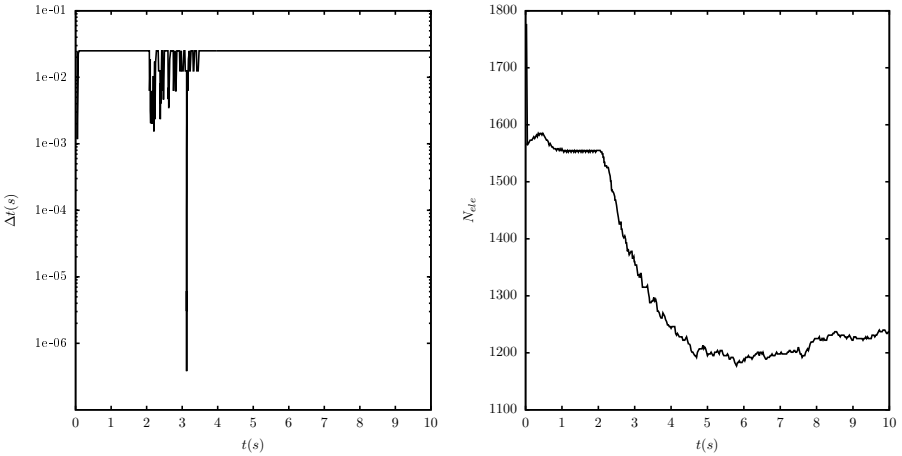

Figure 26: Steenhauer's test case, evolution along time of time steps (left) and number of elements (right)

References

[1]

[2]

[3] Mary Anderson, William Woessner, and Randall Hunt. *Applied Ground Water Modeling: Simulation of Flow and Advective Transport*. August 2015.

[4] Gordon S. Beavers and Daniel D. Joseph. Boundary conditions at a naturally permeable wall. *Journal of Fluid Mechanics*, 30(1):197–207, October 1967. doi:10.1017/S0022112067001375.

[5] M. Bayani Cardenas and Vitaly A. Zlotnik. Three-dimensional model of modern channel bend deposits. *Water Resources Research*, 39(6), 2003. doi:10.1029/2002WR001383.

[6] Daniel Caviedes-Voullième, J. Murillo, and Pilar Garcia-Navarro. Numerical simulation of groundwater- surface interactions by external coupling of the 3D Richards equation and the full 2D shallow-water equations. June 2012.

[7] Jean-Baptiste Clément. *Numerical Simulation of Flows in Unsaturated Porous Media by an Adaptive Discontinuous Galerkin Method: Application to Sandy Beaches*. PhD thesis, Université de Toulon, January 2021.

[8] Jean-Baptiste Clément, Frederic Golay, Mehmet Ersoy, and Damien Sous. Adaptive Discontinuous Galerkin Method for Richards Equation. In *Topical Problems of Fluid Mechanics 2020*, pages 27–34, Prague, Czech Republic, February 2020. Institute of Thermomechanics, AS CR, v.v.i. URL: https://hal.science/hal-02507326, doi:10.14311/TPFM.2020.004.

[9] Jean-Baptiste Clément, Frédéric Golay, Mehmet Ersoy, and Damien Sous. An adaptive strategy for discontinuous Galerkin simulations of Richards' equation: Application to multi-materials dam wetting. *Advances in Water Resources*, 151:103897, 2021. doi:10.1016/j.advwatres.2021.103897.

[10] Clint Dawson. A continuous/discontinuous Galerkin framework for modeling coupled subsurface and surface water flow. *Computational Geosciences*, 12(4):451–472, December 2008. doi:10.1007/s10596-008-9085-y.

[11] Olivier Delestre. *Simulation Du Ruissellement d'eau de Pluie Sur Des Surfaces Agricoles*. PhD thesis, Université d'Orléans, July 2010.

[12] Nathan Delpierre, Hadrien Rattez, and Sandra Soares-Frazao. Finite-volume coupled surface-subsurface flow modelling in earth dikes. *Journal of Hydraulic Research*, 61(5):754–763, September 2023. doi:10.1080/00221686.2023.2246936.

[13] Marco Discacciati, Edie Miglio, and Alfio Quarteroni. Mathematical and numerical models for coupling surface and groundwater flows. *Applied Numerical Mathematics*, 43(1):57–74, October 2002. doi:10.1016/S0168-9274(02)00125-3.

[14] Marco Discacciati and Alfio Quarteroni. Navier-Stokes/Darcy Coupling: Modeling, Analysis, and Numerical Approximation. *Revista Matemática Complutense*, 22, July 2009. doi:10.5209/rev_REMA.2009.v22.n2.16263.

[15] Qinge Dong, Di Xu, Shaohui Zhang, Meijian Bai, and Yinong Li. A hybrid coupled model of surface and subsurface flow for surface irrigation. *Journal of Hydrology*, 500:62–74, September 2013. doi:10.1016/j.jhydrol.2013.07.018.

[16] Mehmet Ersoy, Omar Lakkis, and Philip Townsend. A Saint-Venant Model for Overland Flows with Precipitation and Recharge. *Mathematical and Computational Applications*, 26(1):1, March 2021. doi:10.3390/mca26010001.

[17] R. Allan Freeze and R. L. Harlan. Blueprint for a physically-based, digitally-simulated hydrologic response model. *Journal of Hydrology*, 9(3):237–258, November 1969. doi:10.1016/0022-1694(69)90020-1.

[18] Alex Furman. Modeling Coupled Surface–Subsurface Flow Processes: A Review. *Vadose Zone Journal*, 7(2):741–756, May 2008. doi:10.2136/vzj2007.0065.

[19] Vivette Girault and Béatrice Rivière. DG Approximation of Coupled Navier–Stokes and Darcy Equations by Beaver–Joseph–Saffman Interface Condition. *SIAM Journal on Numerical Analysis*, 47(3):2052–2089, January 2009. doi:10.1137/070686081.

[20] William J. Layton, Friedhelm Schieweck, and Ivan Yotov. Coupling Fluid Flow with Porous Media Flow. *SIAM Journal on Numerical Analysis*, 40(6):2195–2218, January 2002. doi:10.1137/S0036142901392766.

[21] Fabien Marche. Derivation of a new two-dimensional viscous shallow water model with varying topography, bottom friction and capillary effects. *European Journal of Mechanics - B/Fluids*, 26(1):49–63, January 2007. doi:10.1016/j.euromechflu.2006.04.007.

[22] Andro Mikelic and Willi Jäger. On The Interface Boundary Condition of Beavers, Joseph, and Saffman. *SIAM Journal on Applied Mathematics*, 60(4):1111–1127, January 2000. doi:10.1137/S003613999833678X.

[23] Masaru Morita and Ben Chie Yen. Numerical methods for conjunctive two-dimensional surface and three-dimensional sub-surface flows. *International Journal for Numerical Methods in Fluids*, 32(8):921–957, 2000. doi:10.1002/(SICI)1097-0363(20000430)32:8<921::AID-FLD993>3.0.CO;2-3.

[24] Daniele Antonio Di Pietro and Alexandre Ern. *Mathematical Aspects of Discontinuous Galerkin Methods*. Springer Berlin Heidelberg, 2012. doi:10.1007/978-3-642-22980-0.

[25] Kévin Pons. *Modélisation des tsunamis : propagation et impact*. PhD thesis, Université de Toulon, December 2018.

[26] William J. Pringle, Nozomu Yoneyama, and Nobuhito Mori. Two-way coupled long wave - RANS model: Solitary wave transformation and breaking on a plane beach. *Coastal Engineering*, 114:99–118, August 2016. doi:10.1016/j.coastaleng.2016.04.011.

[27] Béatrice Rivière and Ivan Yotov. Locally Conservative Coupling of Stokes and Darcy Flows. *SIAM Journal on Numerical Analysis*, 42(5):1959–1977, January 2005. doi:10.1137/S0036142903427640.

[28] P. G. Saffman. On the Boundary Condition at the Surface of a Porous Medium. *Studies in Applied Mathematics*, 50(2):93–101, 1971. doi:10.1002/sapm197150293.

[29] K. Steenhauer, D. Pokrajac, and T. O'Donoghue. Numerical model of swash motion and air entrapment within coarse-grained beaches. *Coastal Engineering*, 64:113–126, June 2012. doi:10.1016/j.coastaleng.2012.01.004.

[30] K. Steenhauer, D. Pokrajac, T. O'Donoghue, and G. A. Kikkert. Subsurface processes generated by bore-driven swash on coarse-grained beaches. *Journal of Geophysical Research: Oceans*, 116(C4), 2011. doi:10.1029/2010JC006789.

[31] David Keith Todd. Groundwater Hydrology. *Geological Magazine*, 118(4):442, 1980. doi:10.1017/S0016756800032477.

[32] Joel E. VanderKwaak and Keith Loague. Hydrologic-Response simulations for the R-5 catchment with a comprehensive physics-based model. *Water Resources Research*, 37(4):999–1013, 2001. doi:10.1029/2000WR900272.

[33] Gour-Tsyh Yeh, Hwai-Ping Cheng, Ruth Cheng, Hsin Lin, and William Martin. A Numerical Model Simulating Water Flow and Contaminant and Sediment Transport in WAterSHed Systems of 1-D Stream-River Network, 2-D Overland Regime, and 3-D Subsurface Media (WASH123D: Version 1.0). January 1998.